

---

Unterschrift des Betreuers



TECHNISCHE  
UNIVERSITÄT  
WIEN  
Vienna University of Technology

D I P L O M A R B E I T

# Feasibility of Dual Tracer Positron Emission Tomography using Background Subtraction in Prostate Cancer Patients

unter der Anleitung von

Ao.Univ.Prof. DI Dr. Martin Gröschl

Ausgeführt am Institut für Angewandte Physik der  
Technischen Universität Wien

und

DI Dr. Albert Hirtl

Universitätsklinik für Radiologie und Nuklearmedizin  
Medizinische Universität Wien

durch

Jan-Marc Lieskovsky

Am Krautgarten 20/12  
1220 Wien

---

Datum

---

Unterschrift (Student)

# Acknowledgments

I would like to thank Albert Hirtl for all of this time and patience with me. You were a great help and I will never forget this! Thank you very much and I appreciate everything you have done for me greatly.

Ivo Rausch, thank you for helping me understand basically all of the steps of working on a thesis, especially when one realises that they know nothing.

I want to thank Markus Hartenbach for presenting me with the opportunity and hope the research continues smoothly and further progress is made.

Martin Groeschl, thank you for agreeing to supervise me and look forward to the examination!

Finally, I have to thank all of my family and friends, who I dedicate this thesis to, for all of your support throughout the years and your love and your kindness and the moments we shared and everything actually. You guys are the best!

# Abstract

## Introduction

Positron emission tomography (PET) with two tracers is a novel medical imaging technique which has advantages such as shortening the duration of scans, however PET cannot explicitly distinguish between two tracers as both signals stem from 511 keV photon pairs. The aims of this thesis were to (1) determine the behaviour of  $^{18}\text{F}$  - Fluoroethylcholine (FEC) within the prostate in prostate cancer patients for the time interval of 48 minutes to 71 minutes post injection for patients with prostate cancer and (2) to analyse the feasibility of dual tracer PET using FEC and  $^{68}\text{Ga}$  labelled prostate-specific membrane antigen (PSMA).

## Methods

Two retrospective studies based on PET data were analysed in prostate cancer patients. The first study analysed the stability of FEC by comparing the activity of FEC at two time points (48 and 71 minutes) for 6 patients. The second study involved a static PET acquisition of FEC followed by an injection and dynamic acquisition of PSMA. Signal separation was done by background subtraction, with the assumption (supported by the results from the first study) that FEC remained stable, to obtain values for the estimated PSMA activity. Kinetic modeling was performed to compare obtained parameters between the estimated PSMA activities and one patient who was only administered PSMA.

## Results

The percent change in quantitative values for the whole prostate varied less than 10 % for 4 of the 6 patients in the first study. No significant wash out or wash in was observed. In the second study, the irreversible two-tissue compartment model was the best fit kinetic model

for PSMA. The influx parameter  $K_i$  for all patients had the same order of magnitude for each patient with the value ranging from 0.01 to 0.08  $\text{min}^{-1}$ .

## **Conclusions**

The findings in literature and results from the analysis of the choline stability study suggest that FEC remains trapped within cells, however, a full dynamic PET acquisition of FEC activity is advised. Estimated PSMA activity showed similar values for kinetic parameters with the PSMA only patient, however, issues representing true quantification were discussed as there exists a trade off between the benefits of acquired data with multiple tracer PET and quantification.

# Contents

<b>1</b>	<b>Introduction</b>	<b>1</b>
<b>2</b>	<b>Background</b>	<b>6</b>
2.1	Basics of Nuclear Physics . . . . .	6
2.1.1	Radioactive Decay . . . . .	6
2.1.2	Interaction of Charged Particles with Matter . . . . .	8
2.1.3	Interaction of photons with matter . . . . .	9
2.1.4	Interaction of $\gamma$ rays with matter . . . . .	10
2.2	Positron Emission Tomography . . . . .	13
2.2.1	Detection of Events . . . . .	14
2.2.2	Limitations . . . . .	16
2.2.3	Data Representation . . . . .	16
2.2.4	Image reconstruction . . . . .	17
2.2.5	Corrections . . . . .	18
2.3	Radiopharmaceuticals . . . . .	22
2.4	Time Activity Curves . . . . .	22
2.5	Kinetic Modeling . . . . .	23
2.6	Prostate Cancer Classification . . . . .	26
<b>3</b>	<b>Materials &amp; Methods</b>	<b>28</b>
3.1	Materials and Methods for Choline Stability . . . . .	28
3.1.1	Data Acquisition . . . . .	28
3.1.2	Data Analysis . . . . .	30

3.2	Materials and Methods for the FEC-PSMA Dual Tracer Study . . . .	34
3.2.1	Data Acquisition . . . . .	34
3.2.2	Signal Separation . . . . .	36
3.2.3	Kinetic Modeling . . . . .	39
<b>4</b>	<b>Results</b>	<b>42</b>
4.1	Results from the Choline Stability Study . . . . .	42
4.2	Results from the FEC-PSMA Dual Tracer Study . . . . .	48
4.2.1	Kinetic Modeling . . . . .	50
<b>5</b>	<b>Discussion</b>	<b>54</b>
5.1	Discussion of the Choline Stability Experiment . . . . .	54
5.2	Discussion of the FEC-PSMA Dual Tracer Study . . . . .	58
<b>6</b>	<b>Conclusions</b>	<b>62</b>
<b>A</b>	<b>Choline Stability Study Appendix</b>	<b>64</b>
<b>B</b>	<b>FEC-PSMA Dual Tracer Study Appendix</b>	<b>68</b>
	<b>References</b>	<b>70</b>

# 1 Introduction

Positron emission tomography (PET) is a medical imaging technique used in nuclear medicine. The technique gives quantitative, visual and temporal information of a positron emitting radioactive isotope. The most common field for the use of PET is personalized oncology.

In this application, a molecule is labelled with an isotope, in what is known as a tracer or a radio-pharmaceutical, to study the metabolic activity of tissues *in vivo*. The large breakthrough came attaching an  $^{18}\text{F}$  isotope to glucose in the form of Fludeoxyglucose (FDG) which is the most widely studied and applied radio-pharmaceutical.

Tumors are an abnormal growth of cells and have physiological differences from normal tissue. This allows oncologist to stage and diagnose certain cancers by analysing the change of uptake of a tracer amongst tissues. In the analysis, information about the location, severity and aggressiveness of the carcinomas can be recovered which is helpful, for example, when monitoring how effective a certain therapy is going. Prostate cancer (PCa) is one of the cancers where the use of PET is being applied and investigated. PCa is the second most common cancer in men and the incidence is increasing [1]. Imaging techniques such as magnetic resonance imaging (MRI), ultrasound and computed tomography are routinely used, however, show a low diagnostic accuracy leading under or over treatment [1,2].

Prostate cancer has a slow growth rate in comparison to other cancers and the low uptake of glucose is thought to explain why  $^{18}\text{F}$  - FDG is not a useful tracer, with the exception in very aggressive tumours, for monitoring PCa cells [3,4]. Therefore, new radio-pharmaceuticals are being researched.

Results have been encouraging when labelling choline or choline-derivatives with either  $^{18}\text{F}$  or  $^{11}\text{C}$  [2, 5]. Choline is an essential amino acid and is a precursor for the biosynthesis of phosphatidylcholine and phosphorylcholine which are key components in the cell membrane. This process is known as the Kennedy pathway. It is an established characteristic of cancer cells to show elevated levels of phosphocholine [6]. In the first step of the Kennedy pathway, choline undergoes phosphorylation by the enzyme choline kinase which, in PCa cells, has been shown to have a 48 % overexpression with respect to normal tissue [5, 7–9].

Despite the promising results, there is no definite guideline on choline PET imaging and there is, however, a need for a more specific tracer as the uptake of choline is also seen in other prostate tissue such as benign prostatic hyperplasia (BPH) and inflammation [8]. These limitations lead to over and under-treatment in pre-therapeutic diagnosis.

To address these shortcomings, further research has been promising by a novel method of targeting the prostate-specific membrane antigen (PSMA). PSMA is a trans-membrane protein which is expressed at very high levels in prostate cancer cells compared to other tissues, specifically enhanced levels are found in poorly differentiated (aggressive) and metastatic carcinomas [10–12]. Significantly, PSMA is expressed at very high levels in the neo-vascular regions of tumors and has very low levels of detection throughout the body, with slight expression in organs like the brain, kidney, and the small intestine [10, 13]. PSMA represents an ideal biological target for PET imaging of PCa.

The PSMA inhibitor tracer  $^{68}\text{Ga}$  labelled Glu-urea-Lys(Ahx)-HBED-CC ( $^{68}\text{Ga}$ -PSMA-HBED-CC) is used in monitoring PSMA activity [13]. HBED-CC (N,N'-bis-(2-hydroxy-5 (carboxyethyl)benzyl)ethylenediamine-N,N'-diacetic acid) is a chelator allowing for efficient radiolabelling of  $^{68}\text{Ga}$  [14]. The radio tracer will be referred to as PSMA or  $^{68}\text{Ga}$ -PSMA. A study compared PSMA with  $^{18}\text{F}$  - Fluoroethylcholine (FEC), with the results indicating that PSMA showed a higher contrast and more PCa lesions were detected [15].

This thesis is a part of a study performed at the Department of Nuclear Medicine



at the General Hospital in Vienna, Austria. Hartenbach *et al.* has demonstrated that the use of PET/MR improves diagnostic accuracy for patients with PCa with use of  $^{18}\text{F}$  - FEC [16]. Following these results, the study now aims to investigate the behaviour of PSMA in PCa patients after a PET acquisition of FEC. Henceforth, choline,  $^{18}\text{F}$ -FEC, and FEC will be used interchangeably unless otherwise specified.

The staggered injection of PSMA is administered while the activity of FEC still remains present in the body. The feasibility of quantification of this approach, called dual-tracer imaging, is the focus of this thesis.

PET cannot explicitly distinguish between tracers as both signals stem from 511 keV photon pairs. Tracers do, however, have different biokinetics and depending on the isotope, different radioactive half-lives. The rationale for investigating the dual-tracer approach is in the clinical advantages including reduced scan times, reducing the number of scans, co-registration of the images for each tracer, patient convenience, and saving in costs.

The original proof of principle of the dual-tracer has been shown by Huang *et al.* [17]. The majority of published research is done on phantoms and simulated data [18]. There is very limited published literature with real physiological data, and most publications discuss the trade off between the advantages and the tracer recovery performance [19].

This thesis will analyse two studies to determine the feasibility of the dual tracer approach with real clinical data for patients with PCa. The studies are introduced as follows with details and protocols being described later in the thesis.

### **Choline Stability Study**

The first analysis is from a study that took place in Germany concerning PET only data on patients with primary PCa. The aim of this analysis is to determine a possible change in activity and behaviour of FEC within the prostate for the time period of approximately 40 minutes to 70 minutes post injection (p.i.). This part is essential for validating the signal separation algorithm. In literature, choline PET has been studied in great detail, yet there is no published data within this time range and this

research is connected to Chondrogiannis *et al.* who reviewed  $^{18}\text{F}$  labelled choline in PCa patients [8]. This study will be referred to as the Choline Stability Study.

### **FEC-PSMA Dual Tracer Study**

The second part of the analysis will be on the aforementioned dual tracer study and will be referred to as the FEC-PSMA Dual Tracer Study.

For clinical relevancy, FEC is analysed by standard acquisition protocols and is used for quantification. The PSMA is approached as additional information for the clinician with its potential benefit in a retrospective analysis, including quantification, spatial and temporal information.

For prostate cancer PET imaging a coil is inserted into the patients to increase MRI resolution during the acquisition making it very uncomfortable. The physicians have taken measures to have a short scan time by acquiring FEC activity 40 minutes after the injection for 7 minutes. The PSMA acquisition followed.

### **Structure**

This thesis will begin by stating the ultimate aims of this investigation, followed by relevant background information. This is succeeded by the materials and methods used in the studies and analysis. The results from both studies are then given with discussions and conclusions following. In all of the sections, the choline stability study will precede the FEC-PSMA dual tracer study.

## **Aim**

The aims of this thesis are to (1) determine the behaviour of FEC within the prostate for the time interval of 40 minutes to 70 minutes post injection for patients with prostate cancer and (2) to analyse the feasibility of the dual tracer approach in prostate cancer patients using FEC and PSMA using background subtraction.

## 2 Background

This chapter will describe the relevant background physics and modeling techniques involved in this thesis.

### 2.1 Basics of Nuclear Physics

Matter is composed of atoms. An atom consists of a positively charged nucleus, which contains protons and neutrons, and surrounding negatively charged electrons. Only certain combinations of protons and neutrons are possible due to energetically favourable situations. In total, there are around 270 different combinations which make up stable atoms referred to as nuclides. There are also around 1,400 combinations making up unstable atoms known as radionuclides, which are often artificially formed or, in rare cases, found naturally [20].

#### 2.1.1 Radioactive Decay

Due to the favourable energy conditions, an unstable nucleus attempts to shed excess energy in search of a stable situation. This energy, known as radiation, can be released in different forms and the process is known as radioactive decay. It occurs spontaneously and the rate of decay is proportional to the number of radioactive atoms present,

$$\frac{dN}{dt} = -\lambda N, \tag{2.1}$$

where  $N$  is the number of radioactive atoms present and  $\lambda$  is the decay constant.

The activity  $A$  of a radionuclide is defined as the number of radioactive conversions per unit time,

$$A = \frac{dN}{dt}. \quad (2.2)$$

The unit of activity is the Becquerel,  $Bq$ , which in SI units is  $s^{-1}$ . The integration of Equation (2.2) leads to

$$N(t) = N_0 \cdot e^{-\lambda t}, \quad (2.3)$$

where  $N_0$  is the number of nuclides present at  $t = 0$ .

The term  $e^{-\lambda t}$  is referred to as the decay factor (DF). It describes the fraction of nuclei remaining. Radioactive decay is thus a statistical process which represents the probability of for the decay of a collective of nuclides. The half life of a radionuclide is the amount of time required for half of the nuclides present to decay where the following relationships hold:

$$N(T_{1/2}) = \frac{1}{2}N_0, \quad (2.4)$$

where  $T_{1/2}$  is the half life, and

$$T_{1/2} = \frac{\ln 2}{\lambda}. \quad (2.5)$$

The decaying radionuclide is called the mother nucleus and the resultant nuclei are the daughters. The daughter nucleus can either be stable or again unstable. The radiation can be emitted from the mother through one or more ways which include  $\alpha$ -,  $\beta^-$ -,  $\beta^+$ -,  $\gamma$ -decay, and electron capture.

The principle of positron emission tomography is based on  $\beta^+$ -decay and is discussed in the next section.

## $\beta^+$ decay

$\beta^+$ -decay is the emission of a positron ( $\beta^+$ ), accompanied with an almost massless and charge-less particle (for conservation of energy and momentum) referred to as a neutrino ( $\nu$ ), from a nucleus. A positron is the anti-particle of an electron, in that it has the equivalent mass, but opposite charge.  $\beta^+$ -decay, in essence, is a proton being transformed into a neutron. A generic equation for this decay is show as



where  $A$  is the mass number (number of protons and neutrons),  $Z$  is the atomic number (number of protons),  $X$  is the generic symbol for the element of the mother and  $X'$  is the generic symbol of the daughter.

This type of decay occurs mainly for radionuclides which are rich in protons and the binding energy (energy required to break the nucleus into individual protons and neutrons) of the daughter nucleus is greater than the mothers by a minimum of 1022 keV.

### 2.1.2 Interaction of Charged Particles with Matter

A moving charged particle is surrounded by a Coulomb electric field and as a result interacts with orbital electrons (electrons in atoms) and the nucleus of all atoms which have a Coulomb electric field themselves. This interaction leads to loss of their kinetic energy through collision and radiation. The orbital electrons are considered to be free and to be stationary.

In the case of a positron, this interactions occurs very quickly as the positively charged positron is attracted to orbital negatively charged electrons. For this reason, a positron has a short range in matter.

## Annihilation

The process when a particle collides with its antiparticle is called annihilation. Annihilation of a positron-electron results in the total mass being transformed to one, two, or sometimes three photons. The most probable is the result of two photons.

The energy is given by the Einstein relationship

$$E = mc^2, \quad (2.7)$$

where  $E$  is the energy,  $m$  is the mass of the particle,  $c$  is the speed of light in vacuum.

To ensure the conservation of total charge, total energy and total momentum remain zero, the two photons have an energy of  $m_e c^2 = 0.511 \text{ MeV}$  each and move in opposite directions. The process of  $\beta^+$ - decay along with annihilation is seen in Figure 2-1.

Since the electrons will not always be completely free and stationary, and the positron still has a fraction of kinetic energy left when annihilation occurs, the angle is not always  $180^\circ$ . The range of angles from which this varies from  $180^\circ$  can be approximately normally distributed, and have an angle of  $0.5^\circ$  at full width at half maximum (FWHM) [21].

### 2.1.3 Interaction of photons with matter

The energy of a photon is proportional to the frequency  $\nu$  and is

$$E = h\nu = \frac{hc}{\lambda}, \quad (2.8)$$

where  $h$  is the Planck constant and  $\lambda$  is the wavelength of the photon.

When a photon passes through matter (absorbing media), depending on the energy level, it may interact with the absorber atom as a whole, with its nucleus or with an orbital electron. The photon can either be completely absorbed by the atom, its energy can be transferred to a charged particle or the photon can be scattered. This

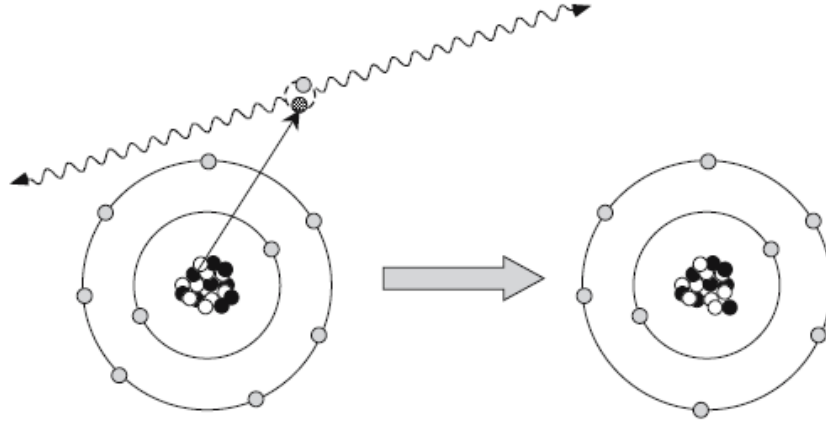


Figure 2-1: An unstable nucleus undergoes positron emission. The positron encounters an electron and they annihilate which gives rise to a pair of approximately anti parallel photons with the characteristic energy of 511 keV [21].

depends on the energies involved.

The linear attenuation coefficient,  $\mu_l$ , is the constant that describes the rate of loss of energy in a medium of a travelling photon. It has the units of  $\text{cm}^{-1}$  and is expressed as

$$I(x) = I_0 e^{-\mu_l x}, \quad (2.9)$$

where  $I(x)$  is the intensity of the photon at depth of  $x$  cm and  $I_0$  is the original intensity.

The emitted pair of photons resulting from annihilation fall into the  $\gamma$  region of the electromagnetic spectrum.

#### 2.1.4 Interaction of $\gamma$ rays with matter

$\gamma$  rays interact with matter through three important interactions; Compton scattering, the photoelectric effect and pair production. The probability for which effect is dominant is dependent on the energy of the incident photons and the atomic number of the absorber.



## Compton Scattering

An interaction of gamma rays with loosely bound electrons of an absorber is called Compton scattering. Orbital electrons can be defined as either loosely bound to the nucleus, where the binding energy of the electron  $E_B$  is small compared to the photon energy  $h\nu$  (i.e.  $E_B \ll h\nu$ ) or they can be tightly bound if this is not the case. For a photon to interact with a tightly bound electron,  $E_B$  must be comparable, but slightly smaller, to  $h\nu$ . The loosely bound electron is considered stationary and free. The result of the Compton effect is a photon of lower energy  $h\nu'$  and an ejected electron, referred to as the recoil electron, which has kinetic energy  $E_K$ .

The angle between the incident photon direction and scattered photon direction is called the scattering angle  $\theta$ . It ranges from the minimum,  $\theta = 0$  (forward scattering) to the maximum  $\theta = 180$  (back scattering). The recoil electron angle  $\phi$  between the recoil electron direction and the incident photon ranges from  $\phi = 0$  to  $\phi = 90$ . Figure 2-2 shows this relationship.

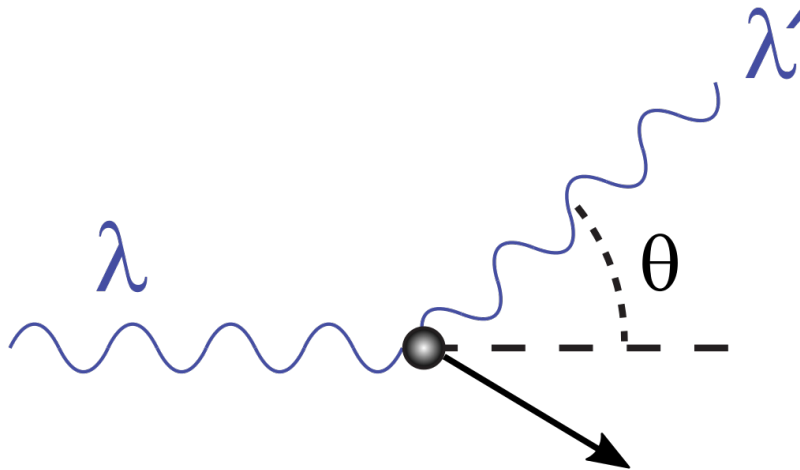


Figure 2-2: Sketch of the Compton effect. The incident photon of wavelength  $\lambda$  interacts with a stationary and free electron resulting in a scattered photon of wavelength  $\lambda'$  and an ejected recoil electron [22].

From relativistic conservation of total energy and momentum, the shift of the wavelength  $\Delta\lambda$  from the incident photon  $\lambda$  to the scattered photon  $\lambda'$  can be calculated and is expressed as

$$\Delta\lambda = \lambda' - \lambda = \frac{h}{m_e c} (1 - \cos \theta). \quad (2.10)$$

Deriving from this relationship the energy of the scattered photon  $E_{\gamma'}$  can be written as

$$E_{\gamma'} = \frac{E_{\gamma}}{1 + \frac{E_{\gamma}}{m_e c^2 (1 - \cos \theta)}}. \quad (2.11)$$

### Photoelectric Effect

An interaction between a photon and a tightly bound electron (unlike Compton effect which is with loosely bound electrons) is called photoelectric effect. In this situation, the total energy of the photon is completely absorbed by the electron. It causes the electron to be ejected with a kinetic energy. This effect has the highest probability of occurring when the magnitudes of photon energy  $h\nu$  and the electron binding energy  $E_B$  are similar.

### Pair Production

If the incident photon energy  $h\nu$  exceeds  $2m_e c^2 = 1.022$  MeV (the combined rest energy of an electron and positron) and it interacts with the Coulomb field of a nucleus (or in rare cases an orbital electron) of absorber atom, it becomes energetically possible to produce a positron-electron pair. All of charge, energy and momentum must be conserved for this effect to occur.

### Linear Attenuation Coefficient

The linear attenuation coefficient  $\mu_l$  for  $\gamma$  rays is dependent on the sum of the Compton effect  $\sigma_C$ , the photoelectric effect  $\tau$  and pair production  $\kappa$  as shown as

$$\mu_l = \sigma_C + \tau + \kappa. \quad (2.12)$$

Figure 2-3 displays the contribution of which effect is dominate on different energy

of gamma photons when interacting with water.

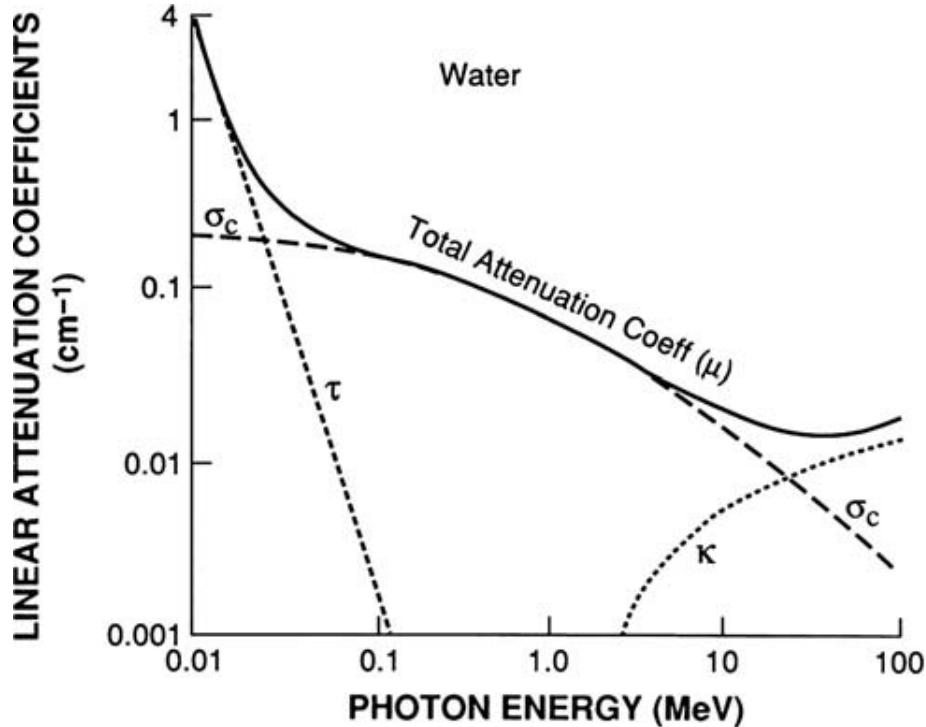


Figure 2-3: Linear attenuation coefficient of  $\gamma$  rays on different energies in water (equivalent to body tissue). The relative contributions of photoelectric, Compton scattering, and pair production processes are illustrated [21].

## 2.2 Positron Emission Tomography

PET is a nuclear medicine imaging technique which allows for 'non-invasive' imaging of the body. The term 'non-invasive' is debated as a radio-pharmaceutical (refer to Section 2.3) must be administered to a patient before undergoing a PET scan.

To obtain an image with PET, data are acquired by a ring of detectors, then through the principle of tomography, an image reconstruction of the original source is attempted.

There are two manners in which PET data are acquired. The most used is a scan which sums up all of the counts, without recording the time of the count, over a period of time is referred to as a static scan. The other method is to record the

time of the events as well and is known as list mode. List mode requires a lot more storage.

The data can be presented as a single static scan or as a dynamic scan, which is a set of static scans in sequences.

PET has been used in the past and in the present less often as a stand alone system. It has become the standard to acquire PET data in a hybrid system with other imaging modalities. The most popular is with Computed Tomography (CT). In addition to anatomical information provided by the CT, it is very accurate when correcting for attenuation as will be discussed shortly. Another hybrid system, which is still very much in its infancy is a PET system in hybrid with Magnetic Resonance Imaging (MRI) and the gantry is known as PET/MR.

### 2.2.1 Detection of Events

Events are detected coincidences (which arises from annihilation). Detectors have been step up in a number of ways and the most used is by having a 360° ring of detectors. Their objective is to capture the  $\gamma$  rays.

A line of response (LOR) is created between opposing detectors when a pair of photons hit the detector within a certain time period,  $\tau$ , known as the coincidence time window.  $\tau$  has an order of magnitude in of  $10^{-9}$  s. The distance the LOR makes from the center is  $s$  and the angle is  $\varphi$ . This, along with the ring of detectors, is illustrated in Figure 2-4.

#### Types of Events

There are different types of events which can be detected:

**True coincidences** This occurs from a positron-electron annihilation where the photons are not significantly scattered resulting in an accurate LOR.

**Scattered coincidences** The photons from the same annihilation are detected, however one or more of the photons are significantly scattered and are not de-

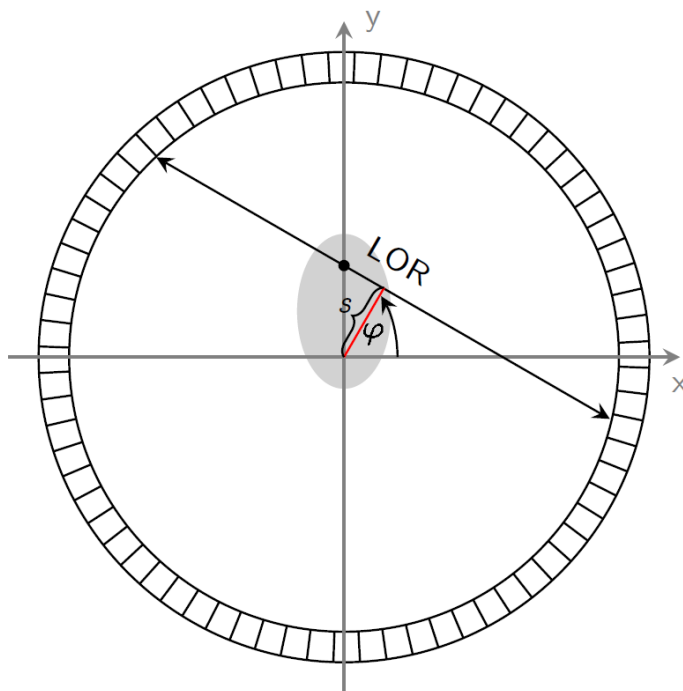


Figure 2-4: A line of response in PET resulting from an annihilation event shown. The detectors are represented by the ring of boxes [Courtesy of A. Hirtl].

tected by the true opposing detectors leading to a false LOR. These lead to noise.

**Random coincidences** Detection of two photons from two different annihilations within the same  $\tau$  leading to a false LOR. These lead to noise.

**Single coincidences** When only one photon reaches the detector from an annihilation. As the PET systems cannot match the photon with another, these events are disregarded. They can arise for small values of  $\tau$ .

**Multiple coincidences** There can occur when more than one annihilation takes places within the  $\tau$  and PET detects the events. These are disregarded.

The summary of events that can be detected are shown in Figure 2-5.

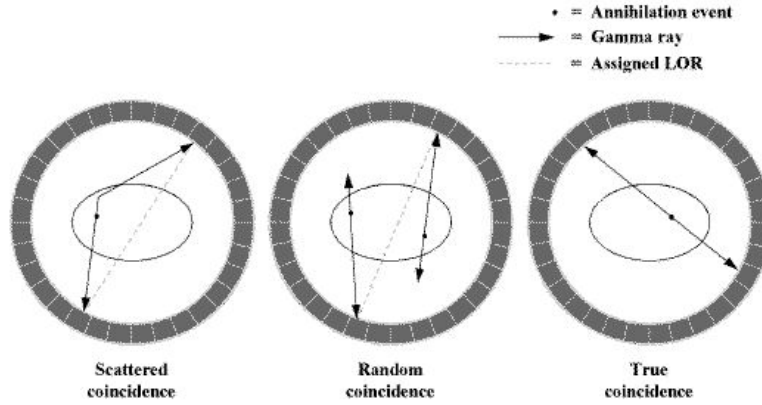


Figure 2-5: Types of coincidences in PET with the assigned LOR. From left to right; scattered, random and true coincidences are displayed [21].

### 2.2.2 Limitations

In addition to scattered and random coincidences, there are two physical limitations. Firstly, the PET detects the point of annihilation rather than the point of decay. The second is that the angle is not exactly  $180^\circ$  as described by 2.1.2, leading to an estimation of the error  $\Delta_{nl}$  as

$$\Delta_{nl} = 0.0022 \cdot D \quad (2.13)$$

where  $D$  is the diameter of the PET scanner [23].

### 2.2.3 Data Representation

Every LOR is stored and most commonly stored in a two dimensional matrix known as a sinogram where the data is represented by polar coordinates after corrections have been made (see Section 2.2.5). In a sinogram, the rows represent the angle  $\varphi$  and the columns represent the displacement  $s$  from the centre for each LOR. The conversion can be written as

$$s = x \cos(\varphi) + y \sin(\varphi), \quad (2.14)$$

where  $x$  and  $y$  are the pixel locations. The intensity for each LOR is represented by the sum of LORs generated (see Figure 2-4).

## 2.2.4 Image reconstruction

After the sinogram is obtained, the idea is to reconstruct the information to make an estimate of the original image. This is accomplished through the theory of back projection. In the discrete version of the back projection operator, we attempt to find a solution for an image with  $m$  pixels by the relationship

$$g_i = \sum_{j=1}^m a_{ij} f_j, \quad (2.15)$$

where  $g_i$  is the sinogram matrix element  $i$ ,  $f_j$  is the image pixel value of the  $i^{\text{th}}$  pixel that is attempted to be recovered, and  $a_{ij}$  is the weighting factor representing the contribution of image pixel  $j$  to the number of counts detected in the sinogram bin  $i$ . Another way to phrase what  $a_{ij}$  represents is the probability that a photon emitted from image pixel  $j$  is detected in sinogram bin  $i$ .

This can be done analytically often using the algorithm called filtered backprojection (FBP) or iteratively using a technique such as the the maximum likelihood reconstruction or the ordered subset expectation maximization (OSEM) [24–26].

### Analytical

In FBP, each pixel element in the sinogram is handled one at a time and is looped over all the projection angles through simple back projections. However, the discrete nature of pixels leads to blurring so a frequency filter in the Fourier transformation of the sinogram bin is applied. The FBP is then the inverse Fourier transform after the application.

## Iterative

Iterative methods attempt to estimate the vector  $f$  that is the solution of Equation (2.15) by using successive estimates. The order of operations is as follows:

1. Make an initial guess for the solution.
2. The forward projections for the current estimate are compared with the measured projections, for each iteration.
3. The result of the comparison is used to modify the current estimate, creating a new estimate.

This is repeated until the values converge. Analytical methods find solutions quicker, however due to noise require frequency filtering with results in a compromise in spatial frequency. Iterative methods are computationally more intensive, but allow for an improved tradeoff between spatial frequency and noise.

## Gaussian Filter

To improve contrast, by smoothing an image, a Gaussian filter is commonly applied. The discrete value in a pixel is distributed as

$$f(x, y) = \frac{1}{2\pi\xi^2} e^{-\frac{(x^2+y^2)}{2\xi^2}}, \quad (2.16)$$

where  $\xi$  is the FWHM. This filter reduces statistical noise, but can lead to the loss of small structures.

### 2.2.5 Corrections

A benefit of PET, apart from spatial information, is that it can give quantitative information as well. This gives physicians information about the metabolism of the tracer. For this reason, it is vital to correct for some sources of error and misleading information. The following will briefly explain the theory behind the corrections.



## Random

The amount of random coincidences  $R$  is related to the amount of single coincidences  $r$  and the coincidence time window by

$$R_{ij} = 2\tau r_i r_j, \quad (2.17)$$

where  $i$  and  $j$  are detector channels for each LOR. The number of single events recorded during a PET acquisition is typically one to two orders of magnitude greater than the number of coincidences which can lead to noisy data. The method of correcting for random which is the most common and relevant to this thesis is known as the delayed coincidence channel estimation. In this method, a second data stream of a coincidence time window much larger (e.g. 128 ns) is collected for each channel. Since a delayed coincidence cannot arise from a true or scattered coincidence, it can only contain random coincidences. This number is subtracted from the number of prompt coincidences (the sum of true, random, and scattered) to yield only true and scattered events. There are two drawbacks of this method. Firstly it contributes to the system's deadtime (described later) and more significantly it can lead to statistical noise. If the ratio of prompt coincidences to the amount of delayed coincidences is high, the noise is not significant. In other cases, the variance of the random distribution is reduced through techniques such as smoothing.

## Normalisation

LORs in PET have different sensitivities for reasons such as detector efficiency and angle between the two detectors. Reconstruction algorithms assume that each LOR has the same sensitivity and therefore these imperfections need to be corrected for prior to reconstruction. This process is known as normalisation.

## Deadtime

Deadtime is defined as the time taken for a system to process subsequent events for them to be registered as separate. As radioactive decay is a random process, there is

a possibility that a coincidence can occur within this time window resulting in a lower level of counts detected. The amount of missed coincidences depends on the system and the activity. Deadtime can account for up to 20% of missed coincidences [?].

## Scatter

The percentage of scattered photons in a PET scan can be up to 40% or more [24]. In a number of Monte Carlo computer simulation studies of the interaction of annihilation photons with tissue resulted that over 80 % of detected photons have only undergone a single scattering interaction [23].

For a  $\gamma$  photon undergoing Compton interaction, can be scattered as much as 45 degrees and lose only 115 keV of its energy as can be calculated from Equation (2.10). For PET systems, the energy window is generally set from 350 and 650 keV. Therefore, scattered coincidences are not easily separated based on their energy. However, a large portion of scattered photons do tend to have lower energies than unscattered as can be seen in Figure 2-6. Methods try to model the scatter distribution are based on this.

## Attenuation Correction

A very important step in obtaining quantitative and accurate images of the activity distribution is to correct for the attenuation for each LOR. The attenuation values vary for different tissue. For a source located at depth  $x$  inside of an object with thickness  $T$ , the probability  $P_{\text{detect}}$  to detect photons  $\gamma_1$  and  $\gamma_2$  is the product of their individual probabilities,

$$P_{\text{detect}} = P_{\text{detect}\gamma_1} \cdot P_{\text{detect}\gamma_2} = e^{-\mu_1 x} \cdot e^{-\mu_1(T-x)} = e^{-\mu_1 T}. \quad (2.18)$$

It can therefore be said that for each LOR, the probability of detection of both photons is only dependent on the thickness between two detectors as displayed in Figure 2-7.

Various methods have been developed to overcome this problem. For PET only

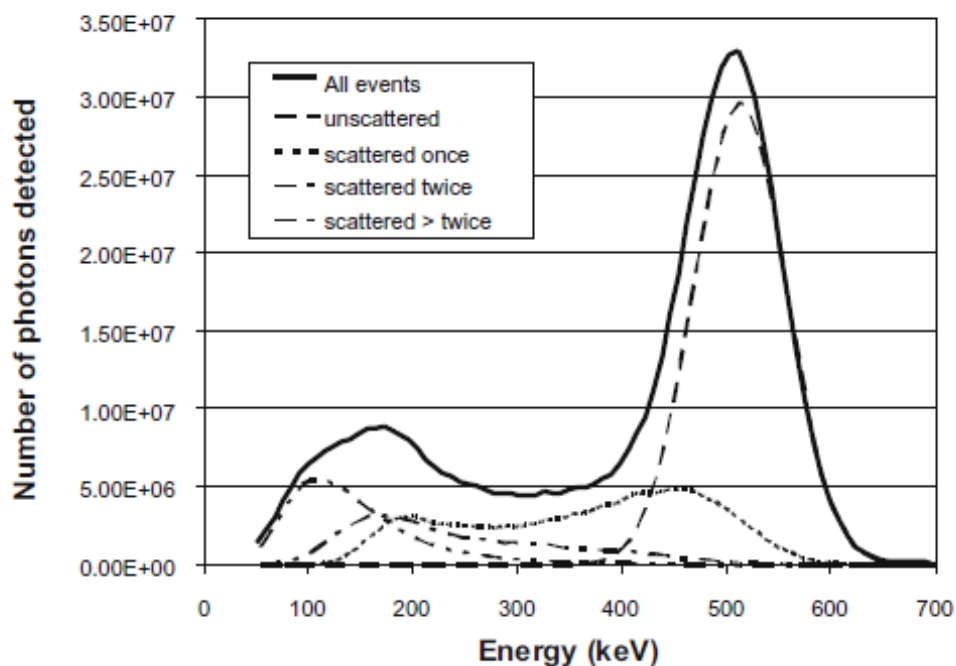


Figure 2-6: Energy spectra of a Monte Carlo simulation of a PET system containing a water based phantom with a positron emitter. A large portion of events detected below the photopeak have been scattered [21].

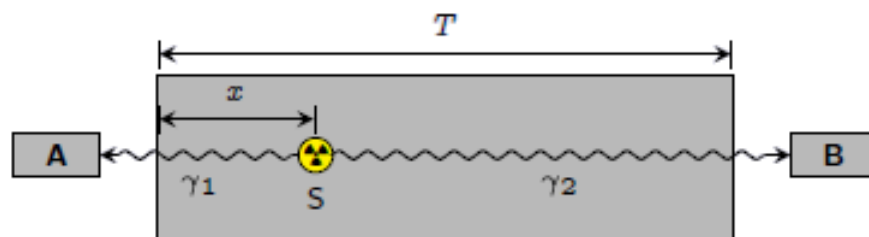


Figure 2-7: Sketch demonstrating the thickness is responsible for attenuation (Courtesy of A. Hirtl).

systems, a positron emitter (commonly a long lived one such as  $^{68}\text{Ge}$  rod) is rotated around the ring of detectors ensuring that each LOR has its intensity distribution recorded. These distributions are used to correct for the attenuation to give a better estimate of the quantitative values. In a PET/CT gantry, CT X-ray photons are used to calculate this using photons of lower energy (60 keV). In the case of the PET/MR gantry, the attenuation correction is calculated based on the Dixon sequence

calculated from the MRI. The Dixon sequence distinguishes between fat tissue and non fat tissue appropriate attenuation values are used.

## Decay

PET data are acquired over periods of time that are not short in comparisons to the isotope half lives. It is therefore necessary to correct for this. The details regarding decay correction are given in Section .

## 2.3 Radiopharmaceuticals

For PET acquisitions, molecules are labelled with positron emitting isotopes and the entire radio-pharmaceutical is metabolised by the body. To minimize radiation dosage for patients, only isotopes with short half lives are considered in nuclear medicine. Thus, many facilities required an on-site cyclotron to produce appropriate isotopes, whereby, for example, the radionuclides are made from the bombardment of protons. Table 2.1 gives the properties of the nuclides used in the studies.

Radionuclide	$T_{1/2}$ [min]	Max Energy of $\beta^+$ [MeV]	Max $\beta^+$ range [(mm) in water]	Mean $\beta^+$ range [(mm) in water]
$^{18}\text{F}$	110	0.64	2.2	0.46
$^{68}\text{Ga}$	68	1.90	9.0	2.15

Table 2.1: Table of properties of two isotopes used in PET [27].

## 2.4 Time Activity Curves

The advantage of the static acquisition, is the significantly smaller amount of data, however, when the data are presented dynamically, it allows one to analyse the behaviour of a tracer at different time points. A graph which displays the activity over different time points is known as a time activity curve (TAC). The TAC can be from a voxel or from a user-defined region of interest (ROI). A method which makes use

of this dynamic information is kinetic modelling which is described in the following section.

## 2.5 Kinetic Modeling

Dynamic PET allows for quantifying the changes in metabolism through a TAC for a given tracer. The physiology of each patient determines the uptake and to translate the measurements of the tracer concentration into meaningful tissue data, an appropriate model of the kinetics of the tracer is needed. This model, in PET tracer kinetics, is called the kinetic model. This provides a useful method to compare the uptake of a tracer for different patients.

The most used kinetic models are compartment models [28]. In compartment modeling, each compartment defines a possible state where the tracer can reside. Between the compartments, there will be a flow of the activity of the tracers involved. These flows are represented by parameters which define the amount of "movement" between the compartments per unit time. Examples of compartments can be the blood (where the tracer is injected), the extracellular space and the intracellular space. The parameters will determine the inflow and outflow of each of the compartments. The ultimate goal is to determine any of these parameters (or rate constants) from tissue measurements.

Figure 2-8 illustrates an example of a two-tissue irreversible model. An irreversible model assumes there is no outflow from the second compartment to the first. In this model there are three rate constants,  $K_1$ ,  $k_2$  and  $k_3$ . The actual flow into tissue is done through the activity in the artery,  $C_A$ .

Other parameters can be calculated from the ones found, for example the influx parameter  $K_i$  which is given by

$$K_i = K_1 \cdot \frac{k_3}{k_2 + k_3}. \quad (2.19)$$

Derived parameters are often referred to as macro-parameters. Due to noisy data, leading to estimated parameters of low precision [29] but with macro-parameters some

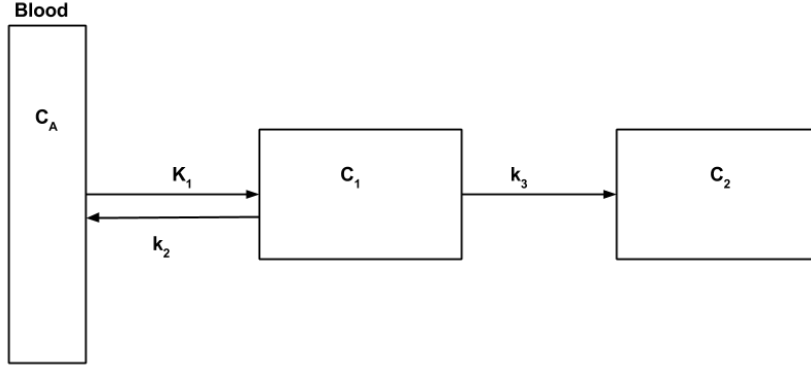


Figure 2-8: A schematic diagram representing an irreversible two-tissue compartment model.  $C_1$ , and  $C_2$  represent the activity concentrations of a tracer in two compartments the tracer can reside.  $C_A$  represent the activity in the artery (whole blood).  $K_1$ ,  $k_2$  and  $k_3$  represent rate constants between the compartments.

of the combinations between the parameters can lead to valuable information.

In the irreversible two tissue compartment model, the measured concentration  $C_{\text{PET}}$  is given by

$$C_{\text{PET}} = C_1(t) + C_2(t), \quad (2.20)$$

where  $C_1(t)$  and  $C_2(t)$  represent the activity in compartments 1 and 2 at time  $t$ , respectively.

Therefore, for both compartments, the activity change can be described with the following differential equations:

$$\frac{dC_1(t)}{dt} = K_1 C_A(t) - k_2 C_1(t) - k_3 C_1(t), \quad (2.21)$$

$$\frac{dC_2(t)}{dt} = k_3 C_1(t). \quad (2.22)$$

To solve these ordinary differential equations we take the Laplace transform with respect to  $t$ , we use the properties  $\mathcal{L}\{C_i(t)\} = \tilde{C}_i(s)$  and  $\mathcal{L}\left\{\frac{dC_i(t)}{dt}\right\} = s\tilde{C}_i(s) - C_i(0)$ . As there is no tracer at  $t = 0$  we set  $C_1(0) = C_2(0) = 0$  and get the following equations:

$$sC_1\tilde{(s)} = K_1 \cdot \tilde{C}_a(s) - (k_2 + k_3)\tilde{C}_1(s) \quad (2.23)$$

$$sC_2\tilde{(s)} = k_3 \cdot \tilde{C}_1(s). \quad (2.24)$$

Now we apply the inverse Laplace transform  $C_i(t) = \mathcal{L}^{-1} \{ \tilde{C}_i(s) \}$  and the property for two Laplace functions  $F(s)$  and  $G(s)$ ,  $(f * g)(t) = \mathcal{L}^{-1} \{ F(s)G(s) \}$ , where  $*$  denotes the convolution operator, we get:

$$C_1(t) = K_1 \cdot \mathcal{L}^{-1} \left\{ \frac{1}{s + (k_2 + k_3)} \cdot \tilde{C}_a(s) \right\} \quad (2.25)$$

$$C_2(t) = k_3 \cdot \mathcal{L}^{-1} \left\{ \frac{1}{s} \cdot \tilde{C}_1(s) \right\}. \quad (2.26)$$

Solving this analytically, we arrive at the solutions for the concentrations of the compartments as:

$$C_1(t) = K_1 \int_0^t e^{(k_2+k_3)(t-u)} C_a(u) du = K_1 e^{(k_2+k_3)t} * C_a(t) \quad (2.27)$$

$$C_2(t) = k_3 \int_0^t C_1(u) du = k_3 * C_1(t). \quad (2.28)$$

What is then attempted is to fit the parameters from the TAC represented by Equation (2.20) using the solutions derived.

For a fitting function  $\hat{y}(t_i, \mathbf{p})$  where  $(\mathbf{p})$  is a set of  $m$  data points, the sum of the squares  $SS$  of the error between the measured data  $y_i$  and the curve fit function  $\hat{y}(t; \mathbf{p})$  is minimized, where

$$SS = \sum_{i=1}^m [y_i - \hat{y}(t_i, \mathbf{p})]^2. \quad (2.29)$$

This can be calculated through numerical methods such as the Levenberg-Marquardt algorithm [30, 31].

## Arterial Input Functions

As the solution of the concentrations of the compartments is based on the convolution with the inflow from the blood, the concentration in the blood is needed. This can be done with sampling the activity in the arteries at different time points or through or it can be estimated by measuring the activity of an artery with the images, this is known as the image derived input function (IDIF).

## Finding a Model

To find a model for a new tracer, there are multiple tests one can use. Unfortunately they are not too robust. However a common test made to see which model fits best is the Akaike information criterion (AIC) [32]. The AIC is given by

$$\text{AIC} = N \cdot \ln(SS) + 2P, \quad (2.30)$$

where  $N$  is the number of frames and  $P$  is the number of parameters. The fit with the lower AIC is considered the "best" fit.

Throughout PET and modeling the units of activity per voxels are in kBq/mL.

## 2.6 Prostate Cancer Classification

Pathologists classify the aggressiveness of a cancer through a score called the Gleason score based on patterns detected. These patterns rate how well PCa cells can be differentiated with normal cells. The pattern is ranked from 1 to 5, with 5 being the most aggressive (poorly differentiated) tumor.

The score is given based on two grades, where the primary is score is given to the dominant pattern (more than 50 % of the total pattern seen). The secondary score is given to the next most frequent pattern seen, which must be less than 50 % of the total pattern seen.

The Gleason score is then counted as the sum of the two patterns. For example a tumor with relatively low aggressiveness could have a pattern  $3 + 3 = 6$  or a highly



aggressive one could have a score of  $4 + 5 = 9$ . PCa with scores  $\leq 6$  usually have a good prognosis [1].

# 3 Materials & Methods

## 3.1 Materials and Methods for Choline Stability

### 3.1.1 Data Acquisition

In order to test how the activity  $^{18}\text{F}$ -FEC behaves in patients with prostate cancer, a retrospective analysis from PET scans from patients with histological confirmed prostate cancer was performed. The data were provided by Dr. Hartenbach. The actual study consisted of three sets of acquisitions for patient. All three acquisitions were followed by a transmission scan used for attenuation correction using  $^{68}\text{Ge}$  rod source. The first acquisition was a dynamic 10 minute scan, followed by a whole body scan and one additional scan of the pelvic region. The analysis dealt with the final two scans as this was the time frame of interest for FEC activity. Unfortunately, data from only six patients were available .

In addition, for 20 patients, standardized uptake values (SUV) at the maximum voxel  $\text{SUV}_{\text{max}}$  and  $\text{SUV}_{\text{mean}}$  (using a 50 % isoconture of a manually drawn ROI) using the software package (Siemens Syngo, Siemens Medical, Erlagen, Germany) were available. The SUV was defined normalized to the body weight as follows

$$\text{SUV [g/ml]} = \frac{\text{measured activity concentration [kBq/ml]} \times \text{body weight [g]}}{\text{injected activity [kBq]}}. \quad (3.1)$$

The ROIs were assessed by two PET-experienced nuclear medicine physicians from the study. These values were used for further analysis and are given in the Appendix

A.

The study was performed on a PET only system and the specifications are shown in Table 3.1. For each subject around 3.3 MBq/kg of body weight of  $^{18}\text{F}$ -FEC was administrated as a bolus through a cubital vein.

The whole body scan began around  $t_* = 25$  mins p.i. at the thorax region and finished at the pelvic region involving a total of 4 bed positions (BP). For each BP, an emission scan for 3 mins was performed followed by a 2 min transmission scan resulting the pelvic region being scanned at  $t_1 = 48 \pm 8$  mins p.i. Finally, the pelvic region was scanned again at  $t_2 = 71 \pm 9$  mins p.i. The protocol relevant to this paper is outlined for clarity in a time-line displayed in Figure 3-1.

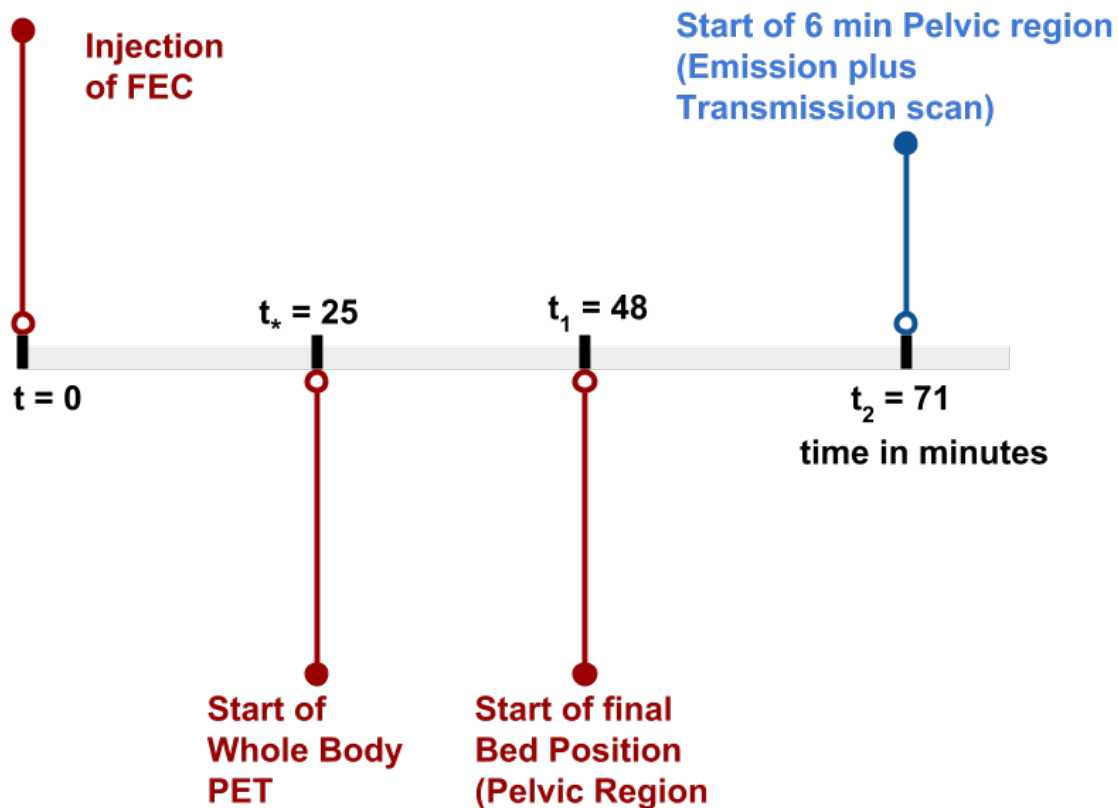


Figure 3-1: Timeline of the relevant PET acquisitions used in the Choline Stability Study analysis.

Image reconstruction was performed using the OSEM algorithm. For the whole body scan, the algorithm consisted of 2 iterations and 8 subsets and 4 iterations and

16 subsets in the later pelvic scan. Random corrections were made with the delayed coincidence channel estimate algorithm and scatter correction was model based. Voxel sizes were 5.15 x 5.15 x 5.15 mm with a total of 128 x 128 pixels for each slice. The number of slices was 125 and 30 for the whole body and later pelvic acquisition, respectively. The images were smoothed for noise using a Gaussian filter such that image resolutions equalled 6-mm FWHM.

Detector Material	Lutetium Oxyorthosilicate (LSO)
Crystal Dimensions	6.45 × 6.45 × 25 mm
Number of Rings	24
Detector Ring Diameter	830 mm
Number of Crystals	9216
Crystals per PMT	16
Axial FOV	162 mm
Transmission Source	3 x <sup>68</sup> Ge 3 x 5 mCi Ge-68 rods
Coincidence time window	6 ns
Max count rate (50% downtime)	850,000

Table 3.1: Specifications of the Siemens ACCEL PET system (Erlagen, Germany).

### 3.1.2 Data Analysis

#### Regions of Interest

The objective of this study was to test the variation between the activity of FEC at two different points ( $t_1$  and  $t_2$ ) in the prostate. To meet this objective a ROI analysis was performed. For each patient, histology results outlined the present tumor and were made by cutting slices of 4 mm in thickness from the apex of the prostate to the base outlining the total thickness of the prostate. The prostate slices were also sliced in quadrants and a typical result is shown in Figure 3-2. The data was in PET only format making it non-trivial to outline the prostate only and therefore a manual ROIs had been drawn for each slice corresponding to the prostate, with the help of the histology. The summation of the ROIs create a volume of interest (VOI) of the whole prostate. An example of the outlining of a prostate can be seen in Figure 3-3.

To help outline the prostate, the activity below 1 kBq/mL was omitted during the outlining.

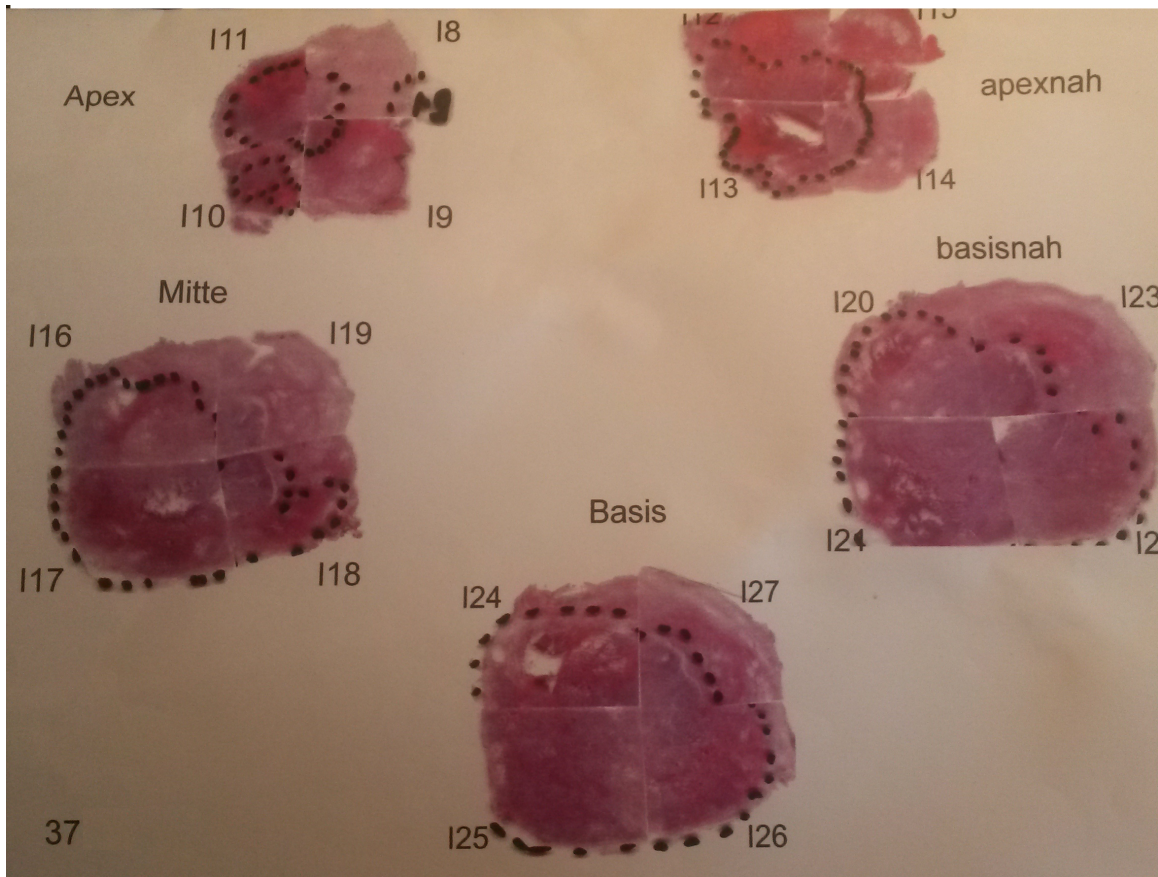


Figure 3-2: A photograph of a typical histology result for a patient.

Automatic definitions of ROI were also calculated using MATLAB (Release 2014b, The MathWorks, Inc., Natick, Massachusetts, USA) as they have shown to improve reproducibility over manual ROI of measured activity concentration [33]. Table 3.2 summarizes all of the defined ROIs along with their abbreviations. Automatic ROIs are not very robust due to the amount of noise and variation for each slice, however possibly the most robust ROI definition is a 3 x 3 voxel centred around the maximum voxel. Four threshold based ROIs were define. The thresholds were set as 50 % of the maximum voxel in the slice and the prostate slice mean. The ROIs were then defines as all voxels with values greater than the threshold, as well as all voxels with values smaller than the threshold.

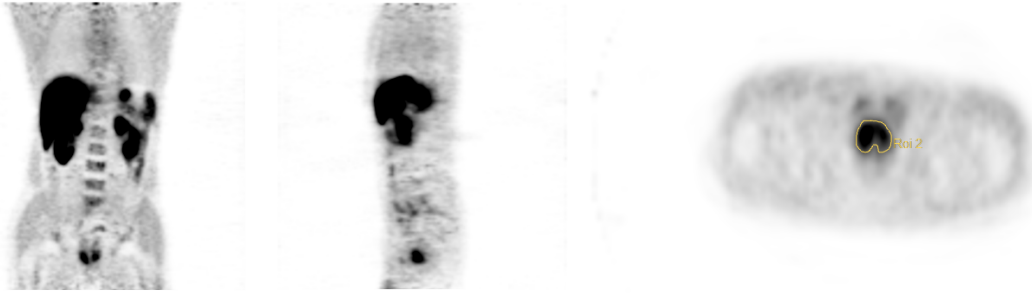


Figure 3-3: An example of the outlining of the whole prostate area of a slice in one of the patient data sets used in the analysis. Left: A coronal view of the whole body scan. Middle: Sagittal view of the whole body scan. Right: Transverse view of a slice containing the prostate where the yellow outlining is taken as the ROI for the whole prostate.

Region of Interest	Abbreviation
Manual whole prostate outline	$ROI_{prostate}$
3 x 3 voxel centered around the maximum voxel	$ROI_{max}$
Activity greater than 50% of the Maximum Voxel	$ROI_{>50}$
Activity smaller than 50% threshold of the Maximum Voxel	$ROI_{<50}$
Activity greater than Prostate slice mean	$ROI_{>\mu}$
Activity smaller than Prostate slice mean	$ROI_{<\mu}$
Activity in the four quadrants separating the prostate	$ROI_{Q1}$

Table 3.2: Table of ROIs used in the analysis of FEC activity.

To increase the chances of not missing a voxel during the delineation of the prostate and for further activity analysis, a quadrant analysis was made. Here the ROIs were defined from the minimum and maximum of the pixels in the x and y directions and splitting in half. In the situation where there were an even number of pixels between the maximum and min in any directions, the extra pixel was a part of the first quadrant ROI. The outlining is shown in Figure 3-4.

All of the ROIs made with their abbreviations used are summarized in Table .

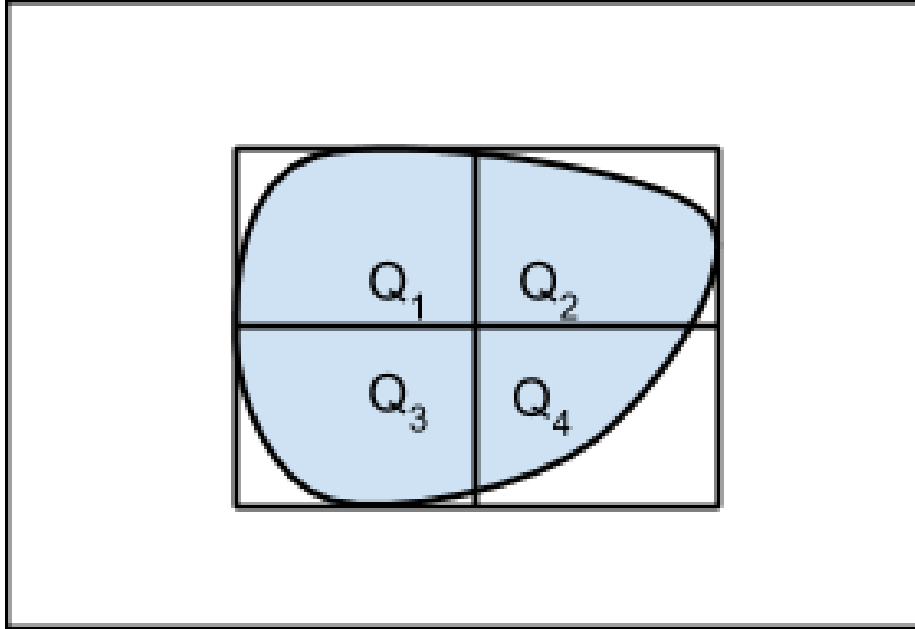


Figure 3-4: Explanation of the quadrant analysis ROI used in the analysis. This is a transverse view of a slice, with Q<sub>1</sub> and Q<sub>2</sub> being anterior to Q<sub>3</sub> and Q<sub>4</sub>.

### **Analysis of the Activity Change**

The decay correction for both sets of data were set to  $t_*$ , the beginning of the whole body acquisition. Decay correction is explained in Section 3.2.2. For each ROI, the total and mean activity was calculated. Using these values, the percentage change was calculated, using the first measurement as the reference value.

Origin (OriginLab, Northampton, MA, USA) was used for statistical analysis using a linear regression analysis and the Pearson correlation coefficient ( $R$ ), where appropriate.

## 3.2 Materials and Methods for the FEC-PSMA Dual Tracer Study

### 3.2.1 Data Acquisition

The objective was to test how feasible the dual tracer approach is with FEC and PSMA for patients with PCa. A retrospective analysis was performed on 8 patients with histological confirmed prostate cancer.

The study involved two sets of PET acquisitions. The first part was a 7 minute static FEC PET acquisition approximately 40 minutes after the tracer administration. This was succeeded by an injection of PSMA with a 40 minute list mode acquisition. The data were taken with the hybrid system of PET and MRI (Siemens Biograph mMR) and the specifications are given in Table 3.3.

Detector Material	Lutetium Oxyorthosilicate (LSO)
Crystal Dimensions	$4 \times 4 \times 20$ mm
Crystal's Per Detector Block	64
Number of Detector Blocks	$8 \times 56 = 448$
Axial FOV	258 mm
Coincidence time window	6 ns

Table 3.3: Specifications of the PET in PET/MR gantry located in Vienna, Austria.

Apart from one patient, each patient was administered 3.0 MBq/kg of choline and all were administered 2 MBq/kg of PSMA. The activity from one patient (patient no. 1), with the omitted FEC, was used as the gold standard to compare for PSMA activity within the prostate.

The time-line of the study is displayed in Figure 3-5.

### Specifications

Image reconstruction was performed by the software system Siemens Syngo (Erlangen, Germany). The OSEM-PSF (point spread function) algorithm was used for image reconstruction with 3 iterations and 21 subsets for both sets of data. The OSEM-PSF



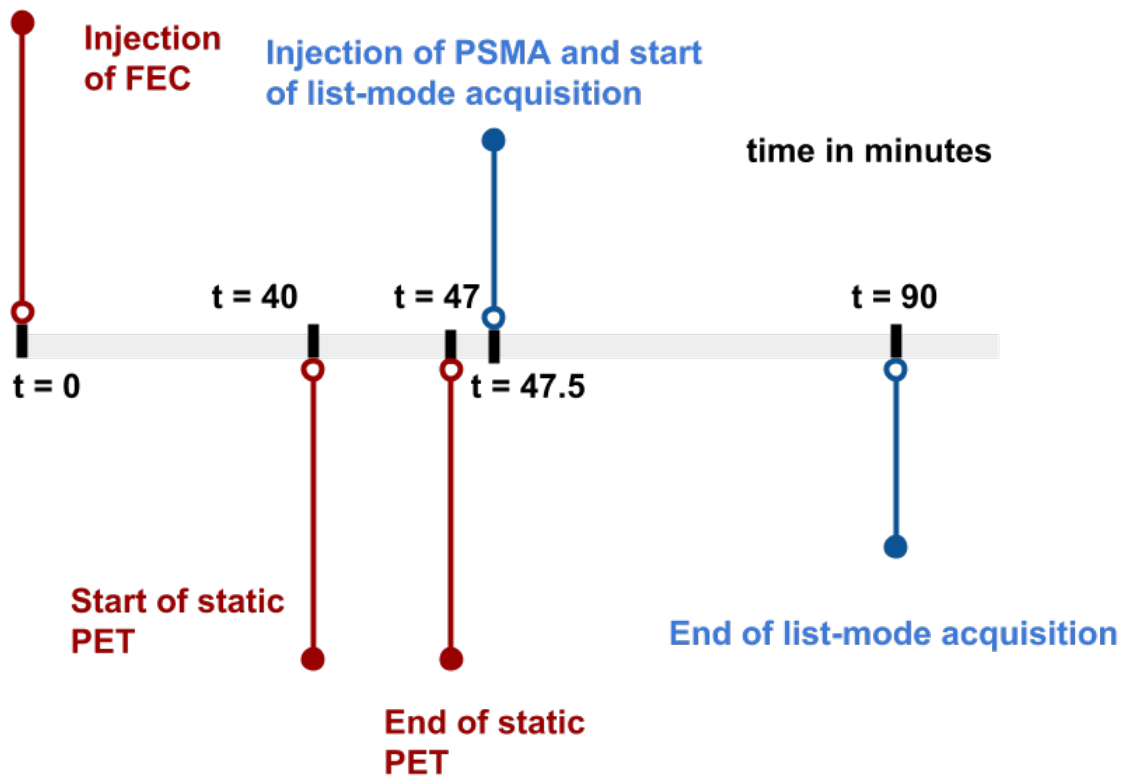


Figure 3-5: The timeline of the FEC-PSMA Dual Tracer Study.

algorithm is an improvement on spatial resolution and noise properties compared with standard iterative reconstruction methods [34].

Random corrections were set with the delayed coincidence channel estimate and scatter correction was model based. The  $\mu$  map created from the Dixon sequence using MRI was used for attenuation correction. Voxel sizes were 2.80 x 2.80 x 2.03 mm with a total of 256 x 256 pixels for each of the 127 slices per frame. The images were smoothed with a Gaussian filter of 3-mm FWHM.

In total there were three reconstructed data sets (two in the case of patient 1) and can be summarized as follows.

1. The data set referred to as the **static acquisition** which consisted of 1 frame of 420 seconds in duration with FEC only and with the system decay correcting for  $^{18}\text{F}$ .

2. The data set referred to as the **dynamic acquisition** which consisted of frames of  $5 \times 60$  seconds followed by  $8 \times 300$  seconds containing both FEC and PSMA and decay correcting for  $^{68}\text{Ga}$ .
3. The **dynamic acquisition** again reconstructed for use of the image derived input function which consisted in frames, in chronological order from the start of the acquisition, of  $1 \times 15$ ,  $3 \times 10$ ,  $5 \times 30$ ,  $2 \times 60$  seconds. This was also corrected for  $^{68}\text{Ga}$ .

Simultaneously, MRI sequences were taken for soft tissue information for the physician. T2-weighted images were used to help locate the tumor, which corresponded to the histology.

### 3.2.2 Signal Separation

Signal separation was done by background subtraction with the assumption that FEC remained stable after 47 minutes to the end of the PSMA acquisition. The method was modified to account for the false decay correction of FEC.

#### Decay Correction

PET data are acquired over periods of time that are not short in comparison to the half lives of the used PET radio-pharmaceuticals. It is therefore necessary to make a correction for the decay which occurs during the measurement. The decay correction must be made for every frame.

The decay curve, based on the decay factor ( $DF$ ), is displayed in Figure 3-6 for an image frame beginning at time  $t$  and ending at time  $t + \Delta t$ . The number of counts recorded is given by the area  $a_d$  (red). The number of counts that would have been recorded in that time without decay is the area  $a_0$  (in blue + red).

The sum of counts during this frame is then

$$a_d = \int_t^{t+\Delta t} e^{-\lambda t} dt = \underbrace{e^{-\lambda t}}_{DF(t)} (1 - e^{-\lambda \Delta t}) \frac{1}{\lambda}. \quad (3.2)$$

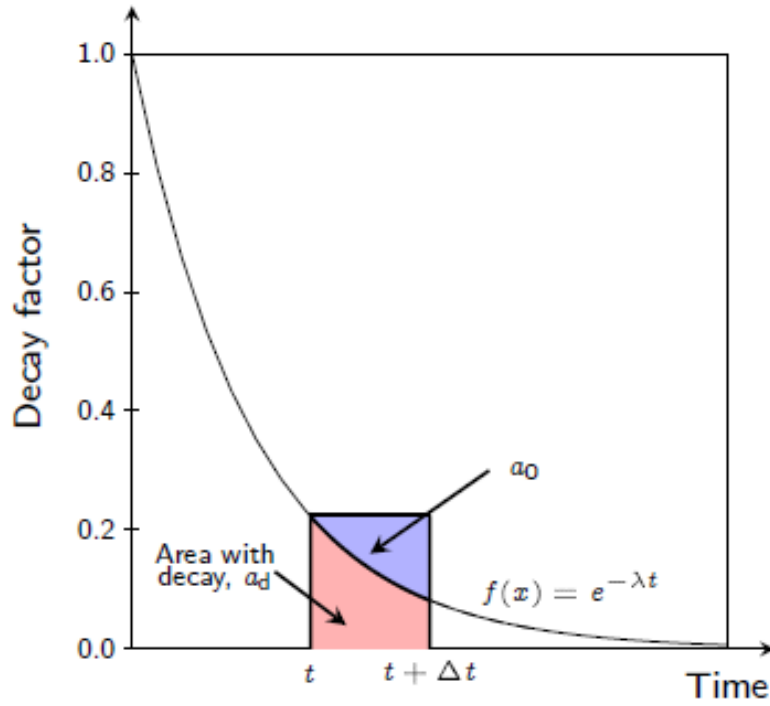


Figure 3-6: Graph of the decay factor (fraction of the number of nuclei remaining) over a period of time.

The sum of counts without decay in this time frame is

$$a_0 = DF(t = t) \times \Delta t. \quad (3.3)$$

Therefore to make the correction for decay for each frame back to the value that it would have been in the absence of decay, the measured activity is multiplied by

$$\frac{a_0}{a_d} = e^{\lambda t} \frac{\lambda \Delta t}{1 - e^{-\lambda \Delta t}}. \quad (3.4)$$

Let  $t_{\text{ref}}$  be the reference time (time of the beginning of the dynamic acquisition) and  $t_{\text{stat}}$  be time at the start of the static acquisition.  $^{18}\text{F}$  and  $^{68}\text{Ga}$  have half lives of 108 minutes and 68 minutes, respectively. This means that the PET system falsely corrected the  $^{18}\text{F}$  isotopes for the half life of  $^{68}\text{Ga}$ , resulting in values greater than the true values (an overcorrection).

To overcome this, the FEC activity during the static scan  $A_{\text{FEC}}(t_{\text{stat}})$  was calculated for decay to the beginning of the dynamic acquisition  $A_{\text{FEC}}(t_{\text{ref}})$  by

$$A_{\text{FEC}}(t_{\text{ref}}) = A_{\text{FEC}}(t_{\text{stat}}) \cdot e^{-\lambda_F \cdot (t_{\text{ref}} - t_{\text{stat}})}, \quad (3.5)$$

where  $\lambda_F$  is the decay constant for  $^{18}\text{F}$ .

$A_{\text{FEC}}(t_{\text{ref}})$  was the activity that was assumed to be stable. For each frame,  $A_{\text{FEC}}(t_{\text{ref}})$  (Equation (3.6)) was multiplied by Equation (3.4) to obtain the activity of FEC calculated by the PET system ( $A_{\text{FEC PET}}$

$$\underbrace{A_{\text{FEC PET}}(t_{\text{frame}})}_{a_0} = \underbrace{A_{\text{FEC}}(t_{\text{ref}})}_{a_d} \cdot e^{\lambda_{\text{Ga}} t_{\text{frame}} - t_{\text{ref}}} \cdot \frac{\lambda_{\text{Ga}} t_{\text{frame}}}{1 - e^{-\lambda_{\text{Ga}} t_{\text{frame}}}} \quad (3.6)$$

where  $t_{\text{frame}}$  is the time at the start of the frame.

The activity of PSMA,  $A_{\text{PSMA}}(t)$  was then estimated by subtraction given by

$$A_{\text{PSMA}}(t) = A_{\text{PET}}(t) - A_{\text{FEC PET}}(t), \quad (3.7)$$

where  $A_{\text{PET}}(t)$  is the measured total activity at time  $t$ .

The process is shown in Figure 3-7 and all of the calculations were performed using MATLAB.

## ROI

ROI analysis was performed by visually delineating the tumor focus using PMOD (PMOD Technologies Ltd, Zürich, Switzerland). The tumors were indicated by the histology results (an example is displayed in Figure 3-8) with the aid of co-registered soft tissue T2- weighted images. Following the delineation, the ROI was then defined as a single iso-contour with a threshold value of 50 % of (maximum voxel - minimum voxel of the delineated tumor). The definitions were performed using the static scan from FEC. The ROI coordinates were then extrapolated for the dynamic acquisition. The exception was with the PSMA only patient, where the dynamic acquisition was used to delineate the tumor.

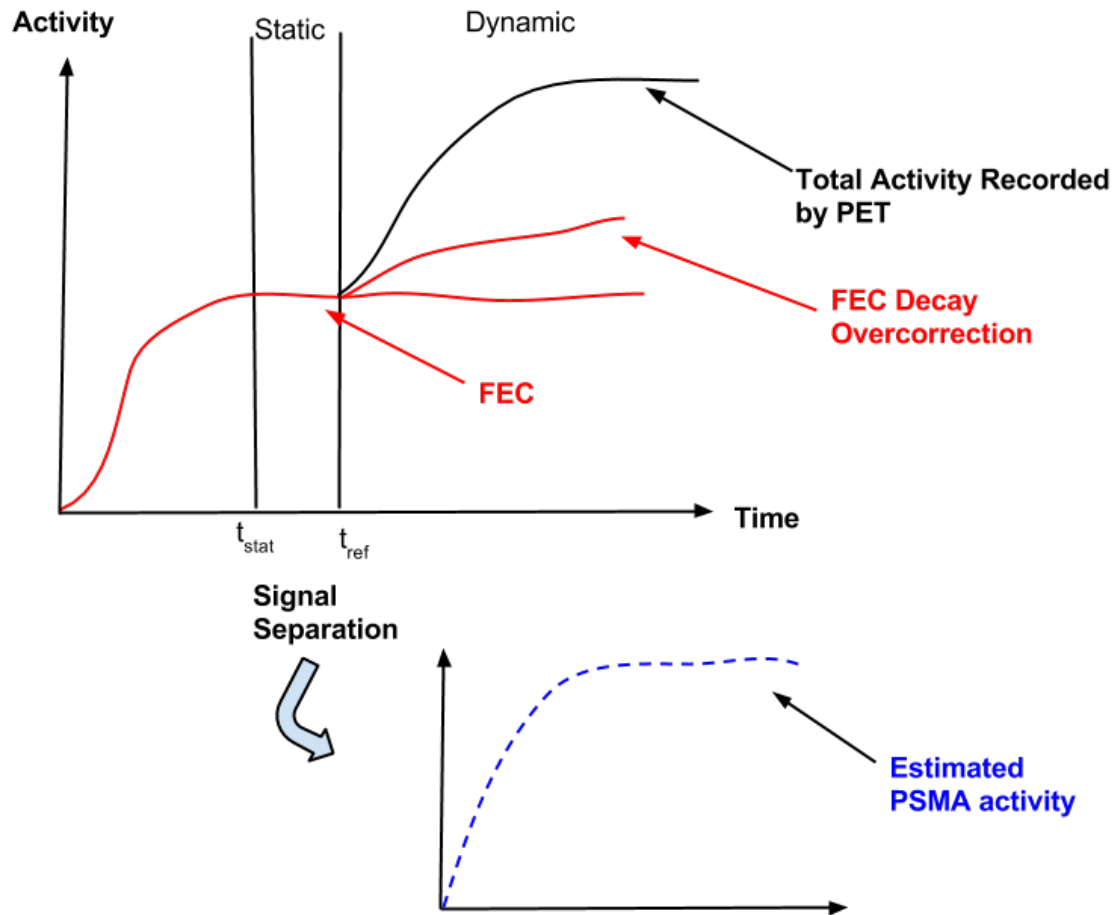


Figure 3-7: The process of staggered injections and the goal of the signal separation to make an estimate of the behaviour of PSMA.

### 3.2.3 Kinetic Modeling

It must be emphasized that the parameters and model is not attempted to give accurate physiological parameters, but rather to see if the parameters between the PSMA-only and the estimated PSMA (after background subtraction) were found.

#### Model Selection

Creating an accurate model for any new tracer is a not a trivial task and would require many PSMA-only patients. Model selection was based on the model best fitting the PSMA only patient based on the model with the lowest Akaike Information

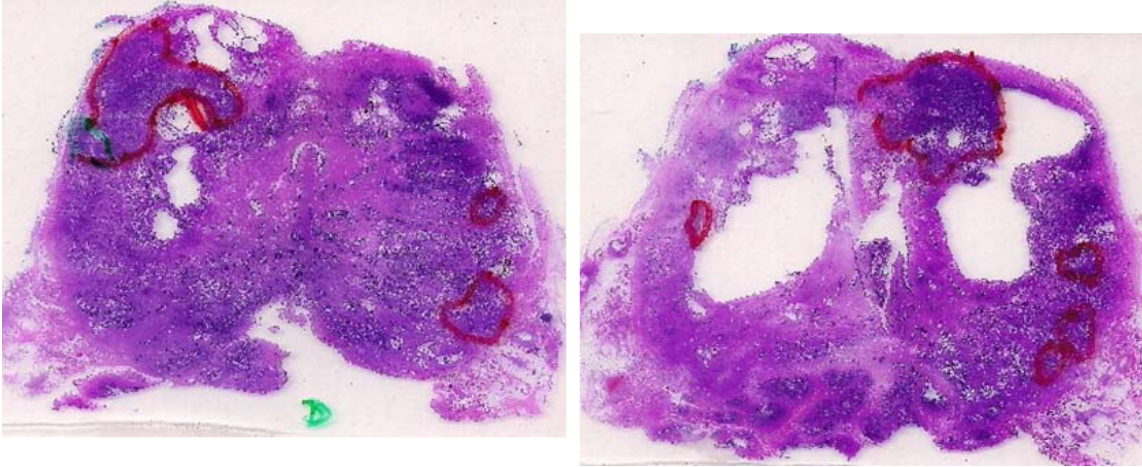


Figure 3-8: An example of two slices from the histology indicating the location of a tumor focus. These areas were used to visually delineate the tumors.

Criterion (AIC). The tested models were the one tissue compartment model, two tissue compartment model and three tissue compartment model for both the reversible and irreversible models.

## **IDIF**

The input function was derived using an ROI centred around the femoral artery using the data set containing the short frames. The ROI was selected by using an 80 % iso contour of the maximum voxel to reduce partial volume and spill out effects as much as possible. For reasons of patient motion, as the artery is very susceptible to small changes, this ROI was defined after the summation of the first 75 seconds. Either the left or the right femoral artery was used for the ROI, this dependent on the higher peak to give a more accurate representation of the input function as recommended by Zanotti-Fregonara1 *et al.* [35]. For each frame and slice, the ROI was then centred around the maximum pixel. The same ROI was then used in the fully dynamic acquisition. The activity of FEC in the artery was not considered significant. As found by Verwer *et al.* the measured concentration of choline in the blood after 40 mins *p.i.* is very low [36].

## **Parameter Estimation**

Kinetic parameter estimation was found through solving the non-linear fit using the Levenberg-Marquardt algorithm to the applied model using PMOD.

# 4 Results

## 4.1 Results from the Choline Stability Study

The stability of Choline was analysed from a total of six patients with PCa. The data presented noisy images and no large wash out or wash in was observed for the patients.

### VOI and ROI Analysis

A volume of interest (VOI) is the summation of ROI for each slice. For the results section, VOI is made from all of the slices that contain the prostate and refer to their respected ROI, e.g.  $VOI_{max} = \sum_{i=1}^n ROI_{max}(i)$  where  $i$  is a slice containing the prostate and  $n$  is total number of slices.

The activity levels of the whole prostate,  $VOI_{prostate}$ , remained stable with an average percent change between the patients of +1 % from  $t_1 = 48 \pm 8$  and  $t_2 = 71 \pm 9$  minutes p.i. For 4 of the subjects, this percent change ranged between  $\pm 9$  %. The VOIs made from the individual  $ROI_{max}$  showed a similar average increase of 9 %. The location of  $ROI_{max}$  for each slice did not differ substantially (all  $ROI_{max}$  were within 1 voxel of each other in the two time-pints).

Large differences were observed in two of the patients (patients no. 4 and 6) and were nevertheless taken into account (see Section 5.1). The percent changes are summarized for each patient in Table 4.1. In all of the cases,  $VOI_{max}$  indicated a higher increase in relation to  $VOI_{prostate}$ .



Patient	$VOI_{prostate}$	$VOI_{max}$
no.	(%)	(%)
1	2.2	6.3
2	-9.4	1.2
3	-8.4	-3.5
4	-29.3	-25.3
5	-2.4	-0.4
6	50.8	77.2

Table 4.1: Table of percentage change of activity of FEC for the entire prostate and the region around the max voxel for  $t_1 = 48 \pm 8$  and  $t_2 = 71 \pm 9$  minutes p.i.

For the threshold definitions, at some slices  $ROI_{<50}$  was not possible as all of the voxels were above the threshold level. This omitted any results for  $VOI_{<50}$  and  $VOI_{>50}$ .

The activity, when using the mean of the prostate slice as the threshold, for  $VOI_{>\mu}$  showed an average increase in activity of 12 %.  $VOI_{<\mu}$  showed a change in activity of  $-12$  %. The two patients with the large differences observed were the only outliers in the absolute change, however both saw a higher and smaller activity change for  $VOI_{>\mu}$  and  $VOI_{<\mu}$ , respectively. This is indicated in Figure 4-1.

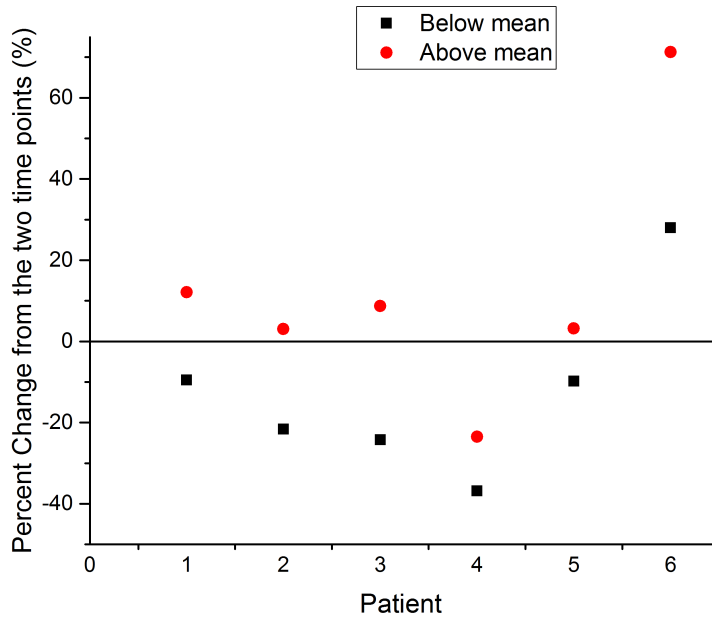


Figure 4-1: The percentage change of the VOIs that were defined by the threshold by the prostate slice from from  $t_1$  to  $t_2$ .

The same behaviour was found a high correlation ( $R = 0.9$ ) when comparing the changes for each slice. This is represented in Figure 4-2, where the abnormally high values (values that showed a percentage increase over 25 %) correspond to patients 4 and 6.

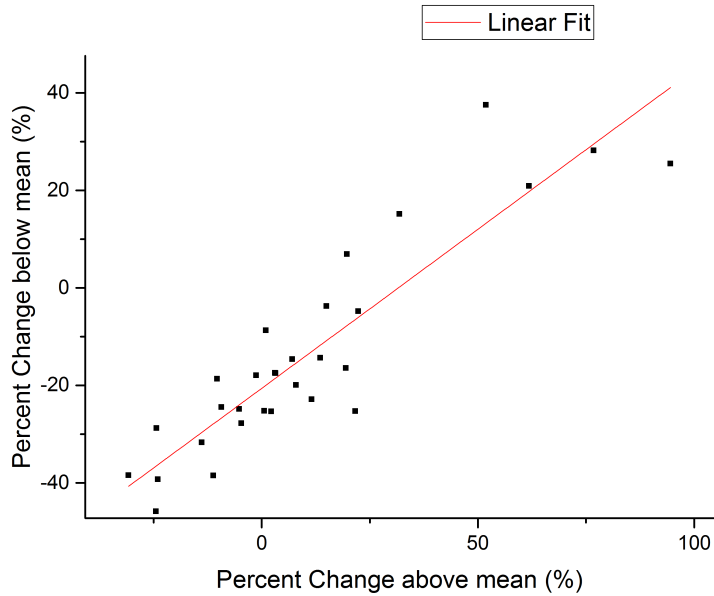


Figure 4-2: A linear fit of the percentage change of each ROI that was defined by the threshold by the prostate slice from  $t_1$  to  $t_2$ .

### Example results for a patient

For clarity, results for a patient are now demonstrated.

For patient no. 4, the one observed to have the largest decrease in activity, an atypical result, the activity of a slice containing the prostate for both time points is displayed as a surface plot in Figure 4-3. Despite the relative large difference in quantitative values, the prostate region (see Table 4.1), including the tumor are clearly visible and no large washout is seen. These slices also demonstrate the variation of two local maxima, and how their quantitative values can be highly affected, possibly by noise.

For patient no. 3, a typical result, the change in activity for  $ROI_{prostate}$  and  $ROI_{max}$  are shown in Figure 4-4. In this patient, slice 5, containing the apex of the prostate, showed an increase in activity, whereas the rest of the prostate showed an almost stable or slight decrease.

In the same patient the change in activity for the quadrants,  $ROI_{>\mu}$  and  $ROI_{<\mu}$  is seen in Figure 4-5.

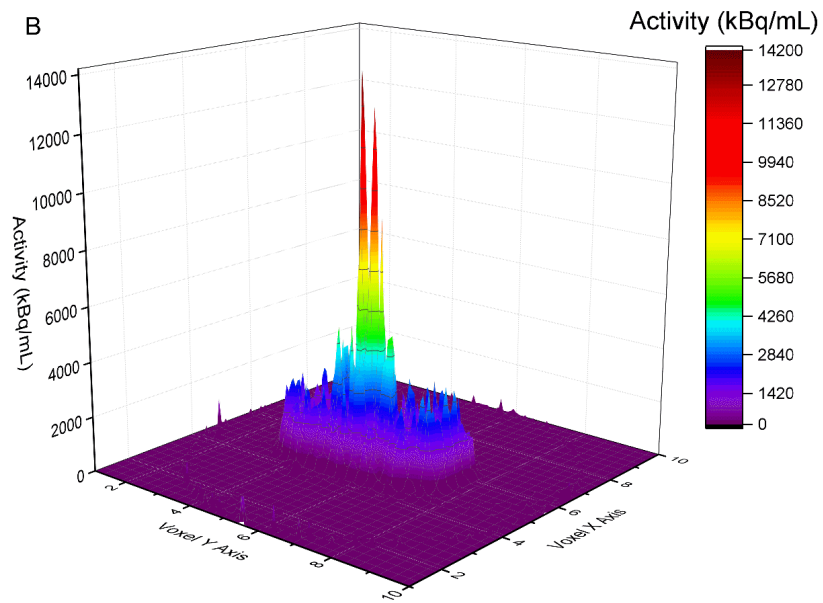
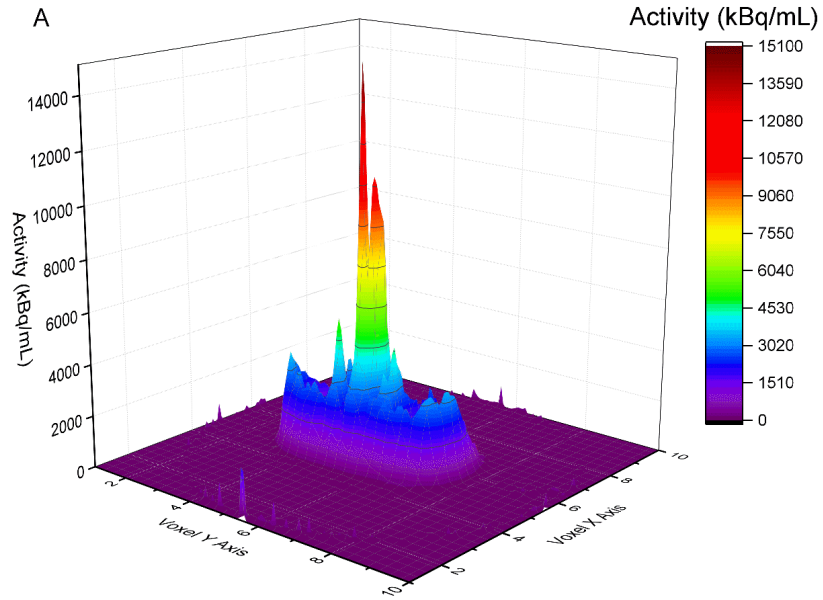


Figure 4-3: A surface plot displaying a typical slice containing the prostate for a patient for two different time points. A)  $t_1$  and B)  $t_2$ .

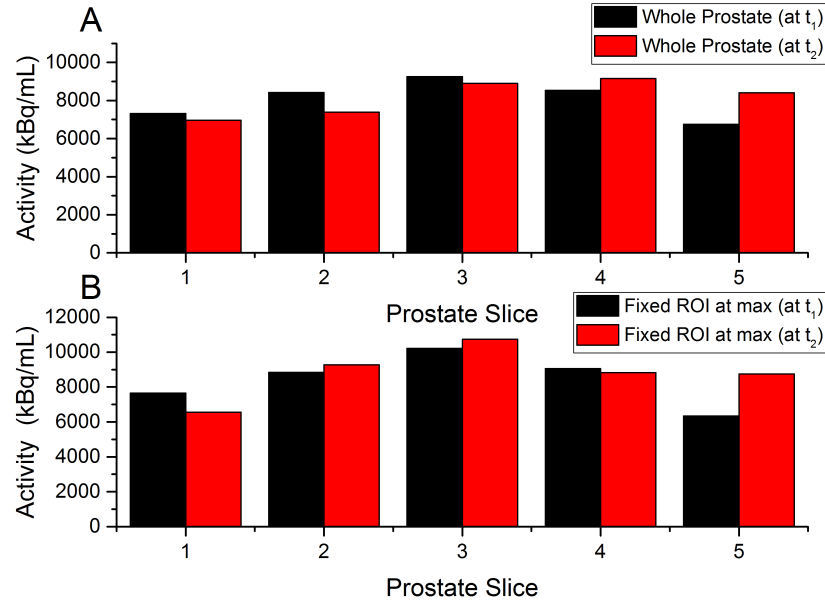


Figure 4-4: Comparison of the activity of FEC of corresponding slices at two different time points for a patient using the whole prostate and voxels surrounding the maximum as region of interests.

### SUV analysis

The average values for  $SUV_{\text{mean}}$  and  $SUV_{\text{max}}$  at 48 mins p.i. were 3.67 and 5.30 and at 70 mins p.i. were 3.52 and 5.08, respectively. Box plots of these are shown in Figure 4-6. The correlation between the  $SUV_{\text{mean}}$  values were slightly higher ( $R = 0.81$ ) than for  $SUV_{\text{max}}$  ( $R = 0.80$ ) when comparing the two time points. The linear fits are seen in Figure 4-7.

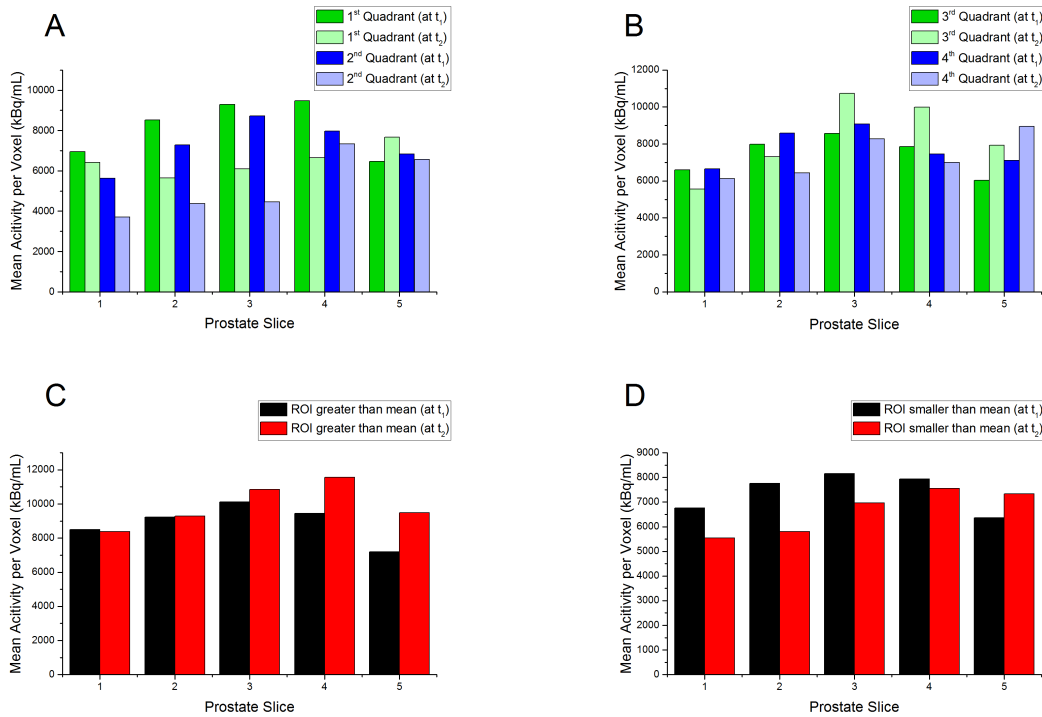


Figure 4-5: Activity of FEC at two time points for various ROI in a patient with PCA. A. ROIs defined by anterior quadrants surrounding the prostate. B. ROIs defined by the posterior quadrants surrounding the prostate. C. Threshold ROI for voxels with activities greater than the whole prostate mean and D. smaller than the whole prostate mean.

## 4.2 Results from the FEC-PSMA Dual Tracer Study

The aggressiveness of the tumors varied among the patients where the post operation Gleason scores are given in the Appendix B. For every ROI surrounding the tumours, a clear large increase in activity was observed, corresponding to the uptake of PSMA. The non-quantitative information presented by the PSMA intake was helpful to the physicians being able to identify the neovascular regions of the tumours. This was confirmed by the histology. The time activity curve for patient 1 (PSMA only) is seen in Figure 4-8. The noise in this this data set was typical for all TACs. The initial peak was present in all of the TACs.

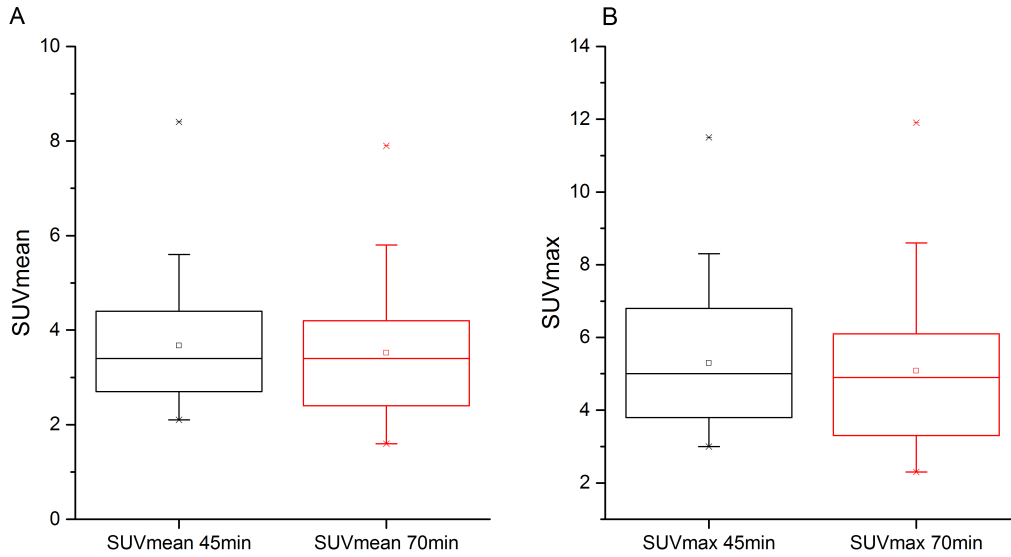


Figure 4-6: Percent change in FEC activity of a ROI centred at the maximum pixel of dimensions  $15.4 \times 15.4$  mm between two time points in a patient with prostate cancer

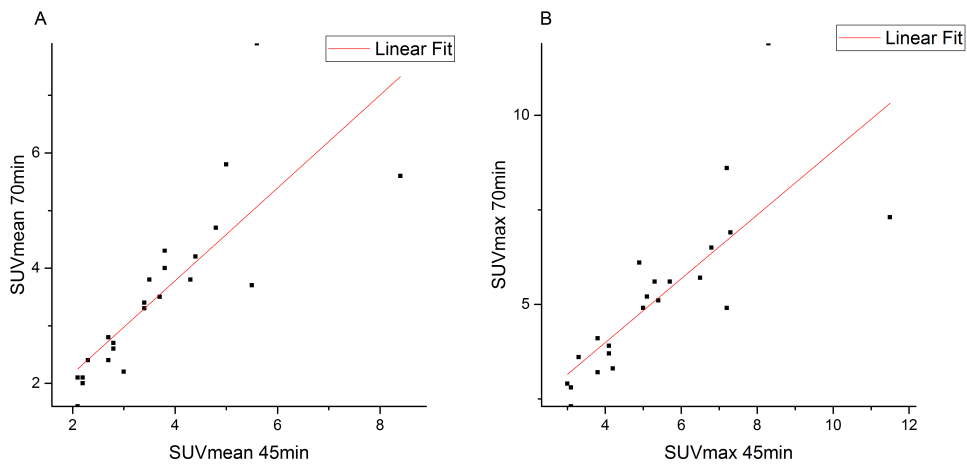


Figure 4-7: Percent change in FEC activity of a ROI centred at the maximum pixel of dimensions  $15.4 \times 15.4$  mm between two time points in a patient with prostate cancer

### Background subtraction

All ROIs could be defined based on the uptake of FEC in the tumors and the histology. After correcting for decay, the activity in the VOIs correlated well with the activity

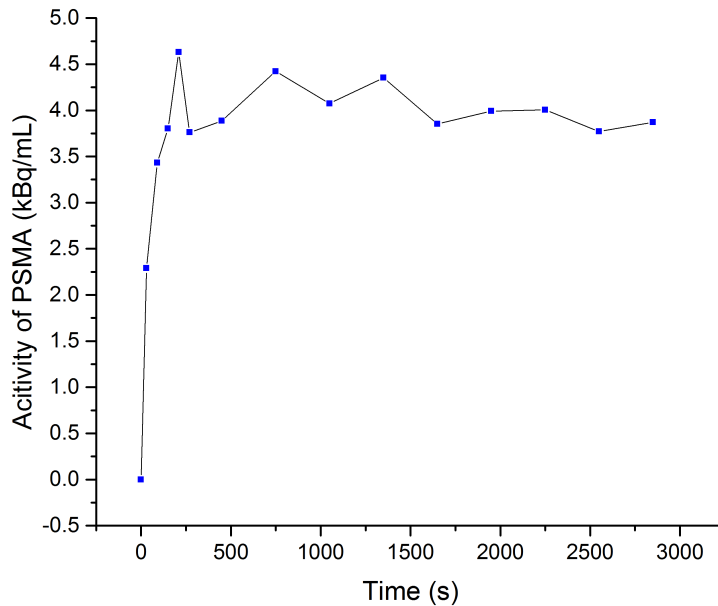


Figure 4-8: The TAC for patient no. 1 who was administered only PSMA.

of the first frame of the PSMA acquisition. Figure 4-9 shows a typical example of the total activity measured for a VOI in the dynamic acquisition. In addition, the estimated FEC and PSMA activity is indicated.

### 4.2.1 Kinetic Modeling

A kinetic model was successfully created for PSMA based on the activity distribution of patient number 1.

#### Image Derived Input Function

For each patient, the femoral artery was located and a ROI was able to be made for each slice. In four patients, three slices were used as the VOI and two slices for the remaining patients. Two typical IDIF can be seen in Figure 4-10. When comparing the IDIF from patient 1 to the rest, There was a strong correlation, ( $R > 0.87$ ) with 5 patients having a correlation coefficient of  $R > 0.93$ . The peak for the IDIF varied for different IDIFs, however all occurred in the third frame, corresponding to the time



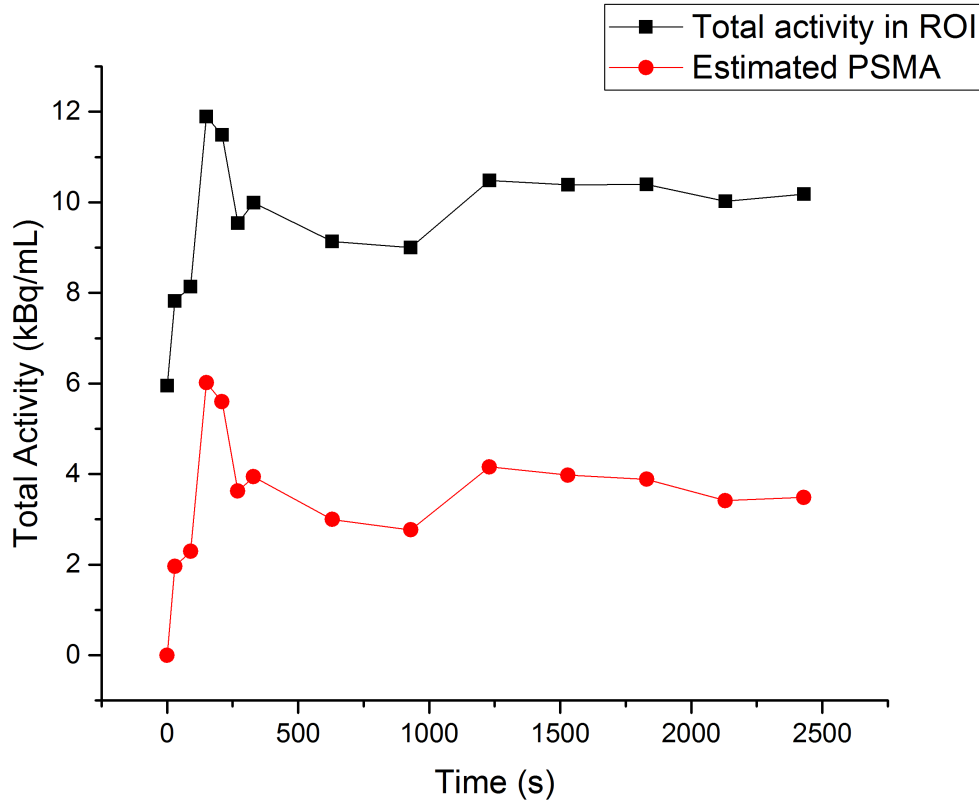


Figure 4-9: A typical background subtraction plot indicating the estimated PSMA activity and the total activity of a VOI.

(in seconds) of  $20 < t \leq 30$  p.i. The activity in all of the IDIFs was very noisy in the time frames corresponding to  $60 < t \leq 300$  p.i. with large fluctuations.

### Model selection

The model which was selected was the two tissue irreversible compartment model displayed in Figure 2-8. For patient one, it resulted in the lowest AIC (37.3) as compared with five other feasible models. For each of the estimated PSMA TAC, this model had the lowest AIC value in respect to the other models. The AIC values are given in the Appendix B.

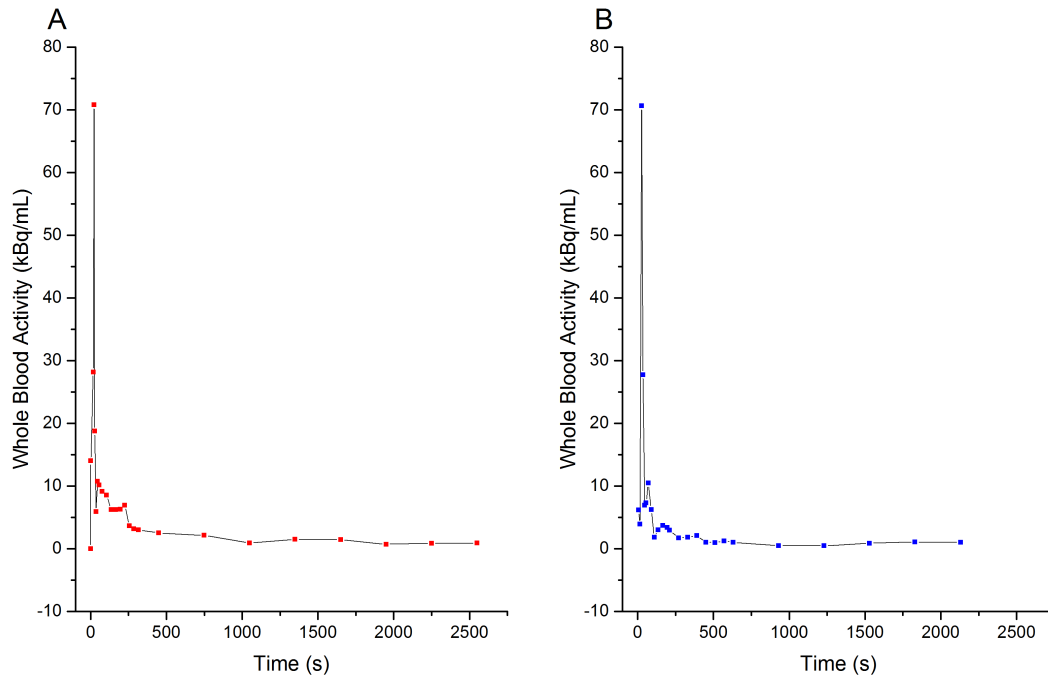


Figure 4-10: Two image derived input functions used in the kinetic modeling of PSMA. A. Patient with the VOI containing PSMA only. B. Patient where the VOI had PSMA and FEC from the administration approximately 47 minutes prior.

### Parameter Estimation

The estimated kinetic parameters from the modeled time activity curves are presented in Table 4.2. The influx parameter,  $K_i$ , showed the same order of magnitude for all of the fitted TACs with its range from 0.01 to 0.08.

Patient no.	$K_1$ mL/min/mL	$k_2$ 1/min	$k_3$ 1/min	$K_i$ mL/mL/min
1	0.18	0.21	0.05	0.04
2	0.16	0.18	0.01	0.01
3	0.14	0.18	0.03	0.02
4	0.15	0.13	0.01	0.01
5	0.26	0.15	0.02	0.03
6	0.67	0.05	0.00	0.03
7	0.23	0.02	0.01	0.08
8	0.36	0.05	0.01	0.06

Table 4.2: Table of kinetic parameters modeling the irreversible two-tissue compartment model for the activity of PSMA.

The parameter percent change from PSMA only is shown in Figure 4-11.

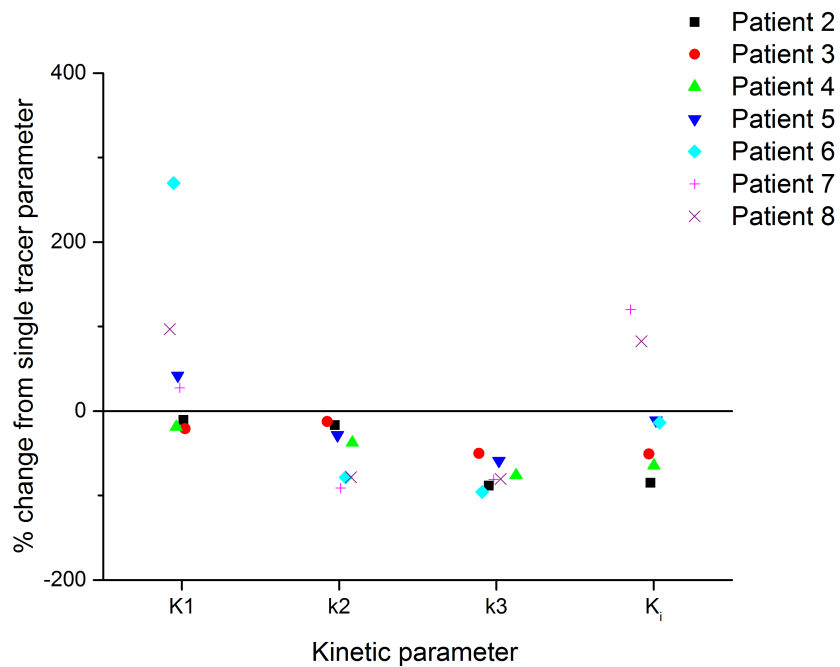


Figure 4-11: Percentage change of parameters from PSMA only.

# 5 Discussion

## 5.1 Discussion of the Choline Stability Experiment

The results show that a large out-flux or in-flux of FEC activity in the time 40 minutes to 70 minutes p.i. is not present. Before any of the physical aspects and limitations of this investigation can be analysed, it is absolutely essential to understand the metabolism and bio-kinetics of  $^{18}\text{F}$ -FEC in patients with PCa for correct interpretation of the images. This is also essential in the analysis of the assumption of choline stability discussed in Section 5.2.

### Behaviour of Choline

There is substantial evidence that choline metabolism is associated with prostate cancer (see Section 1). As mentioned previously, prostate cancer cells contain elevated levels of choline metabolites including phosphocholine and phosphatidylcholine in comparison to normal prostate tissue [2, 37]. Once choline enters the system, it has the task of being transported into the intracellular matrix through the vessels. As soon as choline does enter the cell, the first step of choline metabolism involves the enzyme choline kinase where it undergoes phosphorylation. Eventually the breakdown leads to the major part of the lipid bi-layer. The breakdown and the process is displayed in Figure 5-1.

For the purposes of this paper, the timing of this process is vital. In a study made by Henriksen *et al.* [38] on *in vitro* experiments on human PCa cells, it was concluded that early time points mainly reflect the transport. This was in contrast

to a choline derivative ( $^{18}\text{F}$ -dehydroxylcholine) which cannot be phosphorylated by choline kinase, as it showed similar activity during the early points ( $t < 10$  minutes), however had significantly lower activity at later points suggesting the role of choline kinase in the trapping of choline [38].

The same observation was found by Takesh, where the findings and discussion suggest that the contribution of the uptake of choline at the beginning is due to transport and choline kinase for later times [39]. Furthermore, it was found that a large fraction of choline remains in the cell as unmetabolised [40].

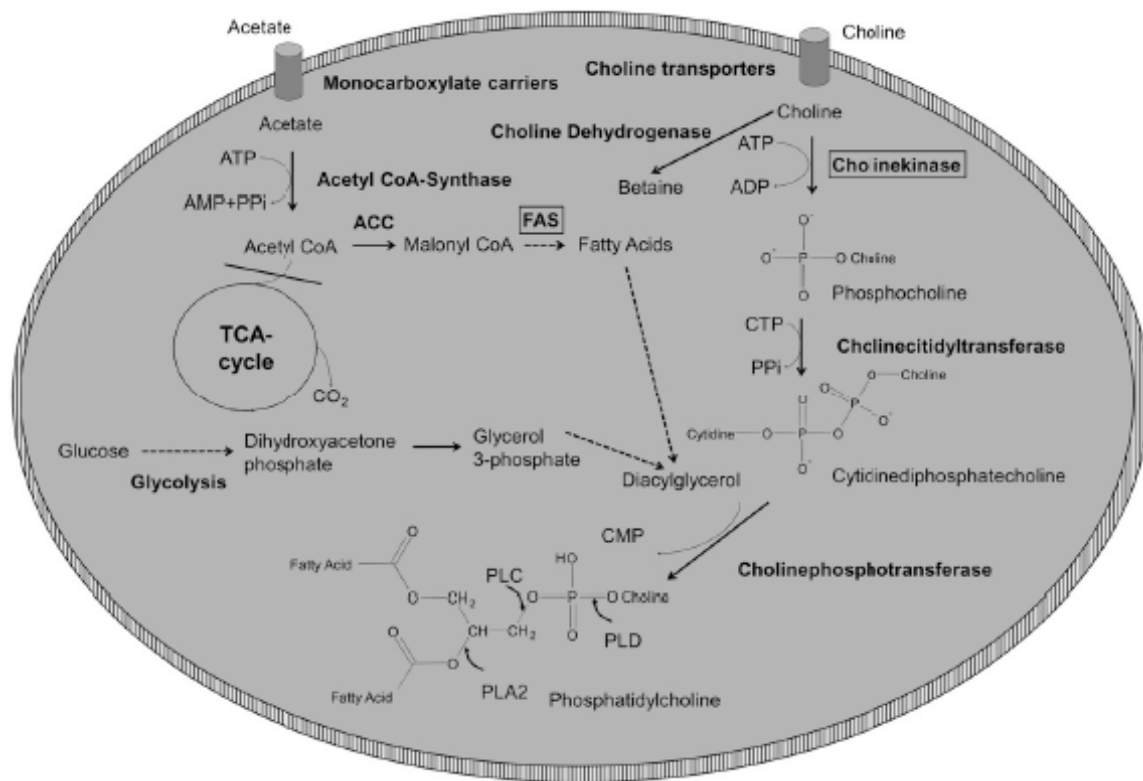


Figure 5-1: A description of the metabolism of choline and acetate in human PCa cells [40].

In a dynamic analysis of the activity of  $^{18}\text{F}$  labelled Flouromethylcholine (FMC) for the first 45 minutes, they found that the kinetic model that best represents FMC is the irreversible two-tissue model [36]. FMC is a different compound to FEC, however they follow similar biodistributions [41].

Additionally a compartmental model based on the distribution of FEC in various

organs (excluding the prostate) for PCa was made from scans up to 4 hours after injection. What was discovered was a very slight wash out in the different organs over the period of time [42].

## Discussion of the results

The findings in literature and results from the analysis of the choline stability study, all suggest that FEC remains trapped within cells.

When using the mean for each prostate slice as the threshold, what perhaps best distinguishes between FEC of high and low activity, the results indicate that for higher activity of FEC, there is an increase of activity relative to the lower activity. This is comparable to the results found by Chokwee where they made a dynamic acquisition in the first 10 minutes after injection and a second static acquisition after 40 minutes. They found that SUV values above a value showed a stable or increase in SUV values and below a decrease [43]. It is then suggested the possibility of benign prostatic hyperplasia or inflammation may be involved in this decrease in activity. The results support that this trend continues after 40 minutes to 70 minutes.

Reproducibility of manually drawn ROIs is difficult. In this analysis, there remains the likely possibility that FEC activity which was not in the prostate was added to the ROI and activity which was in the prostate was missed. To minimize this error, the average was used. It must be noted however, the mean represents various tissues within the prostate that may respond to FEC differently. To compensate for this, further automatic ROIs were made. The most robust method ( $ROI_{max}$ ) is very susceptible to noise, however, it potentially is the best representation of a tumour given its value and size. Using 50% of the maximum as threshold did not have results for many slices as all of the values were above 50 % giving the same results as for the whole prostate. A limitation in the threshold method, including using the mean, is that it represents all of the voxels which had activity larger or smaller and could include different types of cells.

True quantification is a non-trivial task given the amount of variables. A method physicians use is the simplified semi-quantitative value of SUV. In the dynamic study

previously mentioned, it was concluded that SUV had the worse correlation to the actual kinetics of FMC as oppose to other simplification methods [36]. In a simulation study made by Boellard *et al.*, it was found that SUV values have poor accuracy when comparing to ROIs [33]. Therefore one must be sceptical in analysis using the SUV. Despite this, the SUV is one of the most widely used variables in nuclear medicine, and for clinical purposes, it is important to analyse. The SUV analysis agreed that the change between two time-points is low. The method used two different reconstruction settings for the OSEM algorithm creating a potential variation in quantification values. In a study comparing the algorithms, it was found in terms of counts, results are comparable between different algorithms in general, but rather the differences lie in the spatial resolution and blurring [44]. This can have a significant effect on outlining of the prostate.

Noise is always present with real physiological data and stems from many different sources. One such source, and reason for difference in quantification values, comes from patient motion. The patients for the study were asked to stay still in the PET scan for over 75 minutes which is a difficult task and inevitably will have slight movement, possibly explaining the change in locations of some of the  $ROI_{max}$ .

Two patients in the choline study had significant changes. In studies of the kinetics of certain tracers, it is commonplace to omit one or two patients. The reason for this is that some patients respond to pharmaceuticals abnormally. However, as this can happen often, further research (via more patients) should be conducted to deduce whether these two patients were outliers.

For analysis in human participants, obtaining data is a difficult and expensive task. Further analysis with more patient data should be made to come to a more accurate description of FEC activity at later time points. It would be suggested to make multiple fully dynamic acquisitions to overcome some of the limitations in this work.

## 5.2 Discussion of the FEC-PSMA Dual Tracer Study

To begin discussing the meaning of the results found from the dual tracer approach, a summary of the reasoning of the analysis is made.

The focus of this paper is to analyse the feasibility of the background subtraction method for the novel dual tracer approach for the radio-pharmaceuticals of  $^{18}\text{F}$  labelled FEC and  $^{68}\text{Ga}$  labelled PSMA in a retrospective study done on patients with diagnosed prostate cancer.

FEC was measured at 40 minutes post injection, and this acquisition was taken statically as it is difficult to ask a patient to lie in a PET gantry for the full 90 minutes with an MRI coil inserted. This leaves the technical problem and limitation of signal separation algorithms currently being researched to the trivial, background subtraction. This method implies two significant limitations; firstly, any noise accumulated from the static measurement is followed through to later times and secondly, the assumption that the activity of FEC remains completely stable. In practice, these assumptions are not met entirely as there are many physiological factors that cannot be controlled as they vary from patient to patient.

The ROIs made from the choline static images around the tumour corresponded well with the histology results with the aid of the MRI co-registered images. During the dynamic acquisition, noise from the TACs may have resulted from patient motion as the activity of the ROI varied by both increasing and decreasing the activity between frames. It is thought that an improvement in the results could be expected if motion correction algorithms were applied. PET/MR is a novel imaging technique and research into motion correction based on MR sequences could be made and applied in the future. Furthermore, if the histology results would be completely digitalized, fully automatic ROI can be made increasing the reproducibility of the results.

The actual meaning of the kinetic parameters of PSMA is not the focus of this thesis, however, seeing if similar patterns post background subtraction were observed is. There are many assumptions and limitations in selecting a kinetic model for a



new tracer and further PSMA-only data is needed for a true model of the tracer. The model selection was based on the lowest AIC coefficient, which is not the only way to choose a model, and could result in a less accurate model. The parameter of the patient with the most different parameter values (i.e. highest  $K_1$  for example) had the lowest AIC indicated the possibility that with PSMA another model might result in a better representation.

As arterial blood sampling was not possible, the arterial input function for the kinetic model was also based on the IDIF. There are many limitations of the IDIF that can help explain for the model mismatch. IDIF cannot distinguish between plasma activity and whole blood activity and therefore metabolite correction was not taken into account. This is dependent on the tracer. In an analysis of the effectiveness of IDIF, certain papers claim the metabolite fraction for some tracers are negligible [35]. It is then concluded that it must be decided whether errors in concentration levels of up to 25 % can be safely overlooked. An arterial sampling study of PSMA activity is advised to be made for a more accurate description of the arterial input function. IDIF is also very sensitive to noise, partial volume effects and spill out effects increasing room for error. In finding and applying the model, the same method of IDIF was used for all of the patients, hence the accumulated possible errors can only explain the relatively high AIC values when selecting the model.

The parameter most often used to describe irreversible tracers,  $K_i$ , had the most promising results. The low inter-patient variability of the values suggest that the estimated PSMA and the true PSMA followed similar patterns.

PET/MR is a novel imaging technique with limited research. It is appealing to radiologists and the entire nuclear medicine community alike given its lower ionising radiation levels compared with PET/CT and higher soft tissue spatial resolution. The attenuation correction method nevertheless presents itself a limitation. The current method, using the Dixon series based on the phase difference between fat and non fat tissue cannot account for bones. Bones play a significant part in attenuation in relative to other tissue based on its higher linear attenuation coefficient. This a field being largely investigated with some papers reporting some differences in values [45].

Quantification in PET is an issue, quantification with two tracers presents a superior issue. To quantify the PSMA using background subtraction and account for the noise from the FEC study and FEC itself, in the prostate, a significantly higher activity of PSMA would reduce the fraction of noise and FEC values. However, the recommended doses for each tracer do not advise this in the current protocols. Further research should be performed if this would yield similar clinical results.

Additionally for further studies, to achieve more accurate quantification of PSMA activity some alterations to the methods of data collection should be considered. To account for falsely decay correcting the  $^{18}\text{-F}$  isotopes that remained in the body, decay correction could be omitted completely and made to the estimated activities of PSMA and FEC separately.

One possibility is to take the FEC acquisition for a longer duration and in list mode. This may give more information on how the FEC is behaving in the body. Ideally, the entire measurement could be taken in list mode from the moment of FEC injection. Another suggestion would be to wait a longer period between injections (more  $^{18}\text{-F}$  half-lives) allowing for a larger fractions of the isotope to decay. In all of these suggestions there is the significant problem of patient discomfort and if there will be enough volunteers that would undergo such a lengthy study. Image co-registration presents an even larger problem for reasons such as patient motion for scans of such durations. The increased information about the behaviour of choline would allow for more complex signal separation algorithms.

Choline has been shown to be compatible with  $^{11}\text{C}$  which has a shorter half life, however this is not always possible as a cyclotron is required on site.

Andreyev *et al.* demonstrated through Monte Carlo simulations that if the staggered tracer had an additional single gamma emission source, it is able to separate the activities of two tracers with great accuracy based on an expectation maximization algorithm developed [46]. The technology behind this method has yet to be attempted, but massive alterations to the electronics behind PET do not need to be made.

Multi-tracer PET is still very much in its infancy and plenty of research is required.

For all of the above possible alterations, the most important question and debate is if the quantification issues outweigh the benefits of using more than one tracer for a PET acquisition?

## 6 Conclusions

The findings in literature and results from the analysis of the choline stability study suggest that FEC remains trapped within PCa cells in the time-points ranging from the first at 48 minutes and the second at 71 minutes post injection. No significant wash out or wash in was observed between the time interval. The percent change in quantitative values for the whole prostate varied less than 10 % for 4 of the 6 patients. It was found, using the mean as the threshold, that activity increased for voxels greater than the mean by 12 %. For voxels with values less than the mean, the activity decreased by 12 % in all of the 6 patients with histology confirmed prostate cancer. These findings are comparable to literature. There was a strong correlation of  $SUV_{\text{mean}}$  and  $SUV_{\text{max}}$  for 20 patients between the two time-points of  $R = 0.81$  and  $R = 0.80$ , respectively. The results show there is a change, however this change is not clinically important. Given the insufficient amount of data, a suggestion is to make a fully dynamic PET acquisition of FEC activity in this time region.

Each ROI containing tumours showed a clear uptake in activity, which corresponded to the staggered PSMA bolus. The TAC for each patient showed large fluctuations due to noise. The best fit model for PSMA was the irreversible two-tissue compartment model. After estimating the PSMA activity by subtracting the extrapolated FEC activity, the influx parameter  $K_i$  ranged from 0.01 to 0.08  $\text{min}^{-1}$  for the 8 patients indicating similar behaviour. The image derived input function for the patients with estimated PSMA showed very high correlation ( $R > 0.87$ ) with the IDIF from the PSMA only patient. Future studies using background subtraction for the dual tracer should have a significantly larger activity for the second tracer, if possible, to reduce the effect of noise and background activity from the first tracer. Issues

representing true quantification were discussed and there exists a trade off between the benefits of using multiple tracer PET and quantification.

# **A Choline Stability Study Appendix**

SUV <sub>mean</sub> at 48 mins	SUV <sub>mean</sub> at 48 mins	SUV <sub>mean</sub> at 71 mins	SUV <sub>mean</sub> at 71 mins
5.5	7.2	3.7	4.9
8.4	11.5	5.6	7.3
2.1	3.1	2.1	2.8
3.7	5.1	3.5	5.2
2.7	3.8	2.8	4.1
4.8	7.3	4.7	6.9
3.8	4.9	4.3	6.1
3.8	5.7	4	5.6
5	7.2	5.8	8.6
2.8	4.1	2.6	3.9
2.8	4.1	2.7	3.7
5.6	8.3	7.9	11.9
3.4	5	3.3	4.9
4.3	6.5	3.8	5.7
2.3	3.3	2.4	3.6
3.5	5.3	3.8	5.6
2.7	3.8	2.4	3.2
2.2	3	2.1	2.9
4.4	6.8	4.2	6.5
2.2	3.1	2	2.8
3.4	5.4	3.4	5.1
3	4.2	2.2	3.3
2.1	3.1	1.6	2.3

Table A.1: Table of SUV values for patients in the Choline Stability Study

Prostate slice	Prostate kBq/mL	ROIfixed kBq/mL	Abovemean kBq/mL	Belowmean kBq/mL	$Q_1$ kBq/mL	$Q_2$ kBq/mL	$Q_3$ kBq/mL	$Q_4$ kBq/mL
102	7323.14	7656.82	8499.61	6765.87	6949.07	5635.18	6599.49	6647.64
103	8416.41	8842.55	9231.15	7764.62	8520.70	7287.84	7988.96	8587.39
104	9263.06	10210.73	10128.75	8161.28	9297.11	8722.02	8574.86	9084.61
105	8535.95	9052.19	9445.25	7929.75	9481.61	7969.80	7862.20	7454.89
106	6757.58	6336.79	7193.38	6370.20	6463.39	6839.26	6026.11	

Table A.2: Table of average activity for Patient 1 of the FEC stability study on the slices which contain the prostate at the first time point (i.e.  $t_1 = 48$  mins).



Prostate slice	Prostate kBq/mL	ROFixed kBq/mL	Above mean kBq/mL	Below mean kBq/mL	$Q_1$ kBq/mL	$Q_2$ kBq/mL	$Q_3$ kBq/mL	$Q_4$ kBq/mL
14	6970.21	6558.82	8391.58	5548.84	6416.96	3713.13	5566.24	6129.22
15	7386.18	9272.41	9287.09	5802.10	5640.35	4369.45	7311.55	6440.37
16	8904.30	10740.94	10844.33	6964.27	6095.86	4465.99	10734.64	8277.13
17	9153.65	8821.05	11556.68	7551.63	6650.92	7342.11	9987.16	7006.07
18	8410.24	8751.49	9484.32	7336.16	7663.37	6570.19	7936.16	8950.05

Table A.3: Table of average activity for Patient 1 of the FEC stability study on the slices which contain the prostate at the second time point (i.e.  $t_2 = 71$  mins).

# B FEC-PSMA Dual Tracer Study

## Appendix

Patient no.	Gleason Score Post Operation
1	7.50
2	6.00
3	7.00
4	7.00
5	9.00
6	8.00
8	7.50

Table B.1: Table of Gleason Scores for the patients in the FEC-PSMA dual tracer study. The Gleason score was not available for patient 7.

Patient number	MODEL	K1 ml/ccm/min	k2 1/min	k3 1/min	K1/k2 ml/ccm	Flux ml/ccm/min	SumSquared 1/1	ChiSquare 1/1	AIC 1/1
1	2 Tissue Compartments	0.18	0.21	0.05	0.85	0.04	7.50	8.51	37.27
2	2 Tissue Compartments	0.16	0.18	0.01	0.92	0.01	9.32	26.35	50.75
3	2 Tissue Compartments	0.14	0.18	0.03	0.77	0.02	11.93	56.92	60.76
4	2 Tissue Compartments	0.15	0.13	0.01	1.11	0.01	10.09	47.44	58.39
5	2 Tissue Compartments	0.26	0.15	0.02	1.69	0.03	33.03	23.69	60.25
6	2 Tissue Compartments	0.67	0.05	0.00	14.59	0.03	27.64	2.60	17.01
7	2 Tissue Compartments	0.23	0.02	0.01	12.02	0.08	24.52	24.13	63.78
8	2 Tissue Compartments	0.36	0.05	0.01	7.75	0.06	54.04	19.83	52.47

Table B.2: Table of kinetic parameters and results for the Dual Tracer FEC-PSMA study

# References

- [1] Jacob Ramon and Louis J. Denis. *Prostate Cancer*. Springer, 2007.
- [2] S.Schwarzenbock, M. Souvatzoglou, and B.J.Krause. Choline PET and PET/CT in primary diagnosis and staging of prostate cancer. *Theranoistics*, 2:318–330, 2012.
- [3] I.J Liu et al. Fluorodeoxyglucose positron emission tomography studies in diagnosis and staging of clinically organ-confined prostate cancer. *Urology*, 57:108–111, 2001.
- [4] Hossein Jadvar. FDG PET in prostate cancer. *PET Clin.*, 4:155–161, 2009.
- [5] B.J. Krause, M. Souvatzoglou, and U. Treiber. Imaging of prostate cancer with PET/CT and radioactively labeled choline derivatives. *Urol Oncol-Semin O I*, 31:427–435, 2013.
- [6] E. Ackerstaff, K. Glunde, and Z. M. Bhujwalla. Choline phospholipid metabolism: A target in cancer cells? *J Cell Biochem*, 90:525–533, 2003.
- [7] A. Ramirez de Molina, A. Rodriguez-Gonzalez, R. Gutierrez, et al. Overexpression of choline kinase is a frequent feature in human tumor-derived cell lines and in lung, prostate, and colorectal human cancers. *Biochem Biophys Res Commun*, 296:580–583, 2002.
- [8] S. Chondrogiannis, M. C. Marzola, G. Grassetto, et al. New acquisition protocol of 18F-choline PET/CT in prostate cancer patients: Review of the literature

about methodology and proposal of standardization. *BioMed Res Int*, 2014, 2014.

- [9] M. Cimitan, R. Bortolus, S. Morassut, et al. [18F]Fluorocholine PET/CT imaging for the detection of recurrent prostate cancer at PSA relapse: experience in 100 consecutive patients. *Eur J Nucl Med Mol Imaging*, 33:1387–1398, 2006.
- [10] A. Ghosh and W.D. Heston. Tumor target prostate specific membrane antigen (PSMA) and its regulation in prostate cancer. *J Cell Biochem*, 91:528–39, 2004.
- [11] S.M. Hillier et al. Preclinical evaluation of novel glutamate-urea-lysine analogues that target prostate-specific membrane antigen as molecular imaging pharmaceuticals for prostate cancer. *Cancer Res*, 69:6932–40, 2009.
- [12] M. Eder et al. Novel preclinical and radiopharmaceutical aspects of [68] Ga-PSMA-HBED-CC: A new PET tracer for imaging of prostate cancer. *Pharmaceuticals*, 7:779–796, 2014.
- [13] J.R. Osborne et al. Prostate-specific membrane antigen-based imaging. *Urol Oncol*, 31:144–54, 2013.
- [14] M. Eder et al. Tetrafluorophenolate of hbed-cc: A versatile conjugation agent for 68-ga-labeled small recombinant antibodies. *Eur J Nucl Med Mol Imaging*, 35:1878–1886, 2008.
- [15] A. Afshar-Oromich, U. Haberkorn, and M. Eder. 68Ga - gallium-labelled psma ligand as superior PET tracer for the diagnosis of prostate cancer: comparison with 18 F -FECH. *Eur J Nucl Med Mol Imaging*, 39:1085–1086, 2012.
- [16] M. Hartenbach, S. Hartenbach, W. Bechtloff, B. Danz, K. Kraft, B. Klemenz, C. Sparwasser, and M. Hacker. Combined PET/MRI improves diagnostic accuracy in patients with prostate cancer: a prospective diagnostic trial. *Clin Cancer Res*, 20:3244–53, 2014.

- [17] S.C. Huang et al. An investigation of a double-tracer technique for positron computerized tomography. *J Nucl Med*, 23:816–22, 1982.
- [18] D.J. Kadrmas and J.M. Hoffman. Methodology for quantitative rapid multi-tracer PET tumor characterizations. *Theranostics*, 3:757–773, 2013.
- [19] N.F. Black, S. McJames, T.C. Rust, and D.J. Kadrmas. Evaluation of rapid dual-tracer  $^{62}\text{Cu}$ -PTSM +  $^{62}\text{Cu}$ -ATSM PET in dogs with spontaneously occurring tumors. *Phys Med Biol*, 53:217–232, 2008.
- [20] Erwin B. Podgorsak. *Radiation Physics for Medical Physicists*. Springer, 2009.
- [21] D.L. Bailey et al. *Positron Emission Tomography: Basic Sciences*. Springer, 2005.
- [22] [http://en.wikipedia.org/wiki/Compton\\_scattering](http://en.wikipedia.org/wiki/Compton_scattering). accessed on 2015-04-08.
- [23] M. E. Phelps. *PET: Physics, Instrumentation, and Scanners*. Springer, 2006.
- [24] S. R. Cherry, J. A. Sorensen, and M. E. Phelps. *Physics in Nuclear Medicine*. Saunders, 2003.
- [25] L.A. Shepp and Y. Vardi. Maximum likelihood reconstruction for emission tomography. *IEEE Trans Med Imaging*, 1:113–122, 1982.
- [26] H.M. Hudson and R.S. Larkin. Accelerated image reconstruction using ordered subsets of projection data. *IEEE Trans Med Imaging*, 13:601–609, 1994.
- [27] T.F. Brown and N.J. Yasillo. Radiation safety considerations for pet centers. *J Nucl Med Technol*, pages 25–98, 1997.
- [28] A. Peters. A unified approach to quantification by kinetic analysis in nuclear medicine. *J Nucl Med*, 34:706–13, 1993.

- [29] A. Lammertsma. Compartmental modeling in emission tomography. In Claus Grupen and Irne Buvat, editors, *Handbook of Particle Detection and Imaging*, pages 1065–1081. Springer Berlin Heidelberg, 2012.
- [30] K. Levenberg. A method for the solution of certain non-linear problems in least squares. *Q J Appl Mat*, 2:164–168, 1944.
- [31] D. Marquardt. An algorithm for least-squares estimation of nonlinear parameters. *SIAM J Appl Mat*, 11:431–441, 1963.
- [32] H. Akaike. A new look at the statistical model identification. *IEEE Trans Automat Contr*, 19:716–723, 1974.
- [33] R. Boellaard. Effects of noise, image resolution, and ROI definition on the accuracy of standard uptake values: A simulation study. *J Nucl Med*, 45:1519–1527, 2004.
- [34] V. Y. Panin. Fully 3-d pet reconstruction with system matrix derived from point source measurements. *IEEE Trans Trans on Med Img*, 25:907, 2006.
- [35] P. Zanotti-Fregonara, K. Chen, J. Liow, M. Fujita, and R. B. Innis. Image-derived input function for brain PET studies: many challenges and few opportunities. *J Cereb Blood Flow Metab*, 31:1986–1998, 2011.
- [36] E.E. Verwer et al. Quantification of [18]f fluorocholeline kinetics in patients with prostate cancer. *J Nucl Med Mol Imaging*, 2015.
- [37] E. Iorio, D. Mezzanzanica, P. Alberti, et al. Alterations of choline phospholipid metabolism in ovarian tumor progression. *Cancer Res*, 65:9369–76, 2005.
- [38] G. Henriksen, M. Herz, A. Hauser, et al. Synthesis and preclinical evaluation of the choline transport tracer deshydroxy-[18]F-fluorocholeline ([18]FdOC). *Nucl Med Biol*, 31:851–858, 2004.

- [39] M Takesh. Kinetic modeling application to [18]F-fluoroethylcholine positron emission tomography in patients with primary and recurrent prostate cancer using two-tissue compartmental model. *World J Nucl Med*, 12(3):101–110, 2013.
- [40] C Plathow and W. A. Weber. Tumor cell metabolism imaging. *J Nucl Med*, 49:43–63, 2008.
- [41] L. Evangelista et al. [18] F-fluoromethylcholine or [18] F - fluoroethylcholine pet for prostate cancer imaging: which is better? a literature revision. *Nucl Med Biol.*, 42:340–348, 2015.
- [42] A. Giussani, T. Janzen, H. Uusijarvi-Lizana, et al. A compartmental model for biokinetics and dosimetry of [18]F-choline in prostate cancer patients. *J Nucl Med*, 53:985–993, 2012.
- [43] S. A. Kwee, H. Wei, I. Sesterhenn, et al. Localization of primary prostate cancer with dual-phase [18]F -fluorocholeline pet. *J Nucl Med*, 47:262–269, 2006.
- [44] R. Boellaard, A. van Lingen, and A. Lammertsma. Experimental and clinical evaluation of iterative reconstruction (OSEM) in dynamic PET: Quantitative characteristics and effects on kinetic modeling. *J Nucl Med*, 42:808–817, 2001.
- [45] G. Wagenknecht, H.J. Kaiser, F. Mottaghy, and H. Herzog. MRI for attenuation correction in PET: methods and challenges. *Magn. Reson Mater Phy*, 26:99–113, 2013.
- [46] A. Andreyev, A. Sitek, and A. Celler. EM reconstruction of dual isotope PET using staggered injections and prompt gamma positron emitters. *Med Phys*, 41, 2014.